Draft version March 31, 2026
Typeset using LaTeX **twocolumn** style in AASTeX7

arXiv:2508.03912v2 [astro-ph.GA] 27 Mar 2026

When Stars Mimic Monsters: Spectral Evidence for an η Carinae-like Giant Eruption in SBS 0335−052 E

Zixuan Peng (彭子轩) [1], Crystal L. Martin [1], Jiamu Huang (黄嘉沐) [1], Nikolaus Z. Prusinski [2], Chenliang Huang (黄辰亮) [3], Zhuyun Zhuang [2], Yuan Li (李远) [4], Tin Long Sunny Wong [1,5], Jiayang Yang [1] and Joseph F. Hennawi [1,6]

[1] *Department of Physics, Broida Hall, University of California at Santa Barbara, Santa Barbara, CA 93106, USA*
[2] *Cahill Center for Astronomy and Astrophysics, California Institute of Technology, 1216 E. California Boulevard, MC 249-17, Pasadena, CA 91125, USA*
[3] *Shanghai Astronomical Observatory, Chinese Academy of Sciences, Shanghai 200030, People's Republic of China*
[4] *Department of Physics and Astronomy, Texas A&M University, College Station, TX 77843-4242, USA*
[5] *The Observatories of the Carnegie Institution for Science, Pasadena, CA 91101, USA*
[6] *Leiden Observatory, Leiden University, Niels Bohrweg 2, NL-2333 CA Leiden, the Netherlands*

ABSTRACT

SBS 0335−052 E is an extremely low-metallicity ($Z \sim 0.04\,Z_\odot$) blue compact dwarf galaxy. An active galactic nucleus has been proposed to explain the broad Hα emission and near-infrared (NIR) time variability in super star clusters 1 and 2 (SSCs 1&2). However, Peng et al. discovered broad wings in the forbidden [O III] λ5007 emission (up to $\sim 5\,000\,\mathrm{km\,s^{-1}}$), challenging the broad-line region interpretation. We present new KCWI/KCRM integral-field spectroscopy to directly compare spectra across multiple SSCs. The nebula surrounding SSCs 1&2 shows unique features. The Lyβ-pumped O I λ8446 emission constrains $\tau_{\mathrm{Ly}\alpha} \sim 10^8$. Multiple ionization states of iron are detected from Fe^+ to Fe^{+4}. Stellar photoionization models can reproduce the [Fe III]/[Fe II] and [Fe IV]/[Fe III] line ratios at high density ($n_e \sim 10^6\,\mathrm{cm^{-3}}$), but they fail to account for most of the [Fe V] emission. The broad Hα wings exhibit an exponential profile; the asymmetric wings extend from $\sim -5\,000\,\mathrm{km\,s^{-1}}$ to $\sim 10\,000\,\mathrm{km\,s^{-1}}$. Thomson scattering in a radially expanding medium provides a good fit with $v_w \sim 200\,\mathrm{km\,s^{-1}}$, optical depth $\tau_e \sim 10$, and an outer to inner radius of 10. Enhanced N/O and potentially depleted Fe/O ratios are consistent with CNO-cycled ejecta from massive stars and with dust formation, respectively. We propose that mass loss from a massive star interacting with its circumstellar medium drives a shock that powers the NIR variability, the luminous X-ray point source, and the [Fe V] emission. If confirmed, the proposed stellar eruption would be a distant example of an η Carinae-like giant eruption, and the first in an ultra-low metallicity environment.

Keywords: Luminous blue variable stars (944) — Blue compact dwarf galaxies (165) — Galaxy chemical evolution (580) — AGN host galaxies (2017)

1. INTRODUCTION

Unambiguously identifying active galactic nucleus (AGN) activity in low-metallicity dwarf galaxies is highly challenging. Common diagnostics include detecting very-broad (VB) wings (FWHM $\gtrsim 1\,000\,\mathrm{km\,s^{-1}}$) in permitted lines such as Hα (e.g., Y. Harikane et al. 2023; S. Salehirad et al. 2025; I. Juodžbalis et al. 2025), very-high-ionization rest-UV and optical emission lines (e.g., [Ne V]; J. Chisholm et al. 2024; S. Hernandez et al. 2025), and stochastic photometric variability across a wide wavelength range, from X-ray to optical/UV and infrared emission, on timescales of days to years (e.g., M.-H. Ulrich et al. 1997; B. J. Shappee et al. 2014).

However, these diagnostics are not definitive indicators of AGN activity and can also arise from non-AGN processes. For example, any corresponding VB component in forbidden transitions such as the [O III] $\lambda\lambda$4959, 5007 doublet may be too faint to detect (typically $\lesssim 10\%$ of the total line flux; e.g., Z. Peng et al. 2025). This can misclassify purely star-forming galaxies with high-velocity outflows as broad-line AGNs. Moreover, hard stellar radiation fields may mimic the ionizing signatures of AGNs in metal-poor environments (e.g., C. T. Richardson et al. 2025), and similar multi-wavelength time variability can also arise from a η-Carinae like system with a giant eruption phase (i.e., a significant mass-loss episode ejecting $\sim 10-40\,M_\odot$ over

Corresponding author: Zixuan Peng (彭子轩)
Email: zixuanpeng@ucsb.edu

$10-40$ years; K. Davidson & R. M. Humphreys 2012; K. Davidson 2020; K. Weis & D. J. Bomans 2020).

Nearby low-metallicity dwarf galaxies with high signal-to-noise ratio, spatially-resolved spectroscopy and multi-wavelength observations provide key laboratories for offering critical insight into disentangling extreme star formation from AGN activity. In this study, we focus on a local ($z = 0.0135$) blue compact dwarf galaxy SBS 0335-052 E (J0337-0502 hereafter), which has a low stellar mass ($M_* \sim 10^7\,M_\odot$), exceptionally low gas-phase metallicity ($Z \sim 0.03-0.05\,Z_\odot$), and high specific star formation rate ($\log \mathrm{sSFR}\,(\mathrm{yr}^{-1}) \sim -7.40$; see Table 1 for a summary of its main global properties).

S. Hatano et al. (2026, hereafter H26) recently propose the presence of an active massive BH in its super star clusters 1 and 2 (SSCs 1&2; see Figure 1), primarily based on the observed VB Hα component (extending to $\sim 10\,000$ km s^{-1}) and the near-infrared (NIR) variability in the W1 (3.4 μm) and W2 (4.6 μm) bands (i.e., increased by $\Delta f_{\mathrm{W1}} \sim 0.1$ and $\Delta f_{\mathrm{W2}} \sim 0.7$ mJy, respectively, from $\sim$ 57800 to 59600 MJD).

This region also appears as a point source in *JWST*/MIRI (M. Mingozzi et al. 2025) and NICMOS 1.6μm (R. I. Thompson et al. 2009) observations, with detections of very-high-ionization lines such as He II λ4686 (C. Kehrig et al. 2018). It uniquely exhibits dust, H_2, and thermal radio emission (K. E. Johnson et al. 2009) that are not detected in the other SSCs. The luminous X-ray point source ($\sim 3\times10^{39}\,\mathrm{erg\,s^{-1}}$ in the $0.5-10$ keV band; T. X. Thuan et al. 2004) may also originate from this region. Although the X-ray source is located $\sim 0\farcs3-0\farcs7$ north of SSCs 1&2 (magenta circle in Figure 1; A. H. Prestwich et al. 2013), previous studies suggest that this position offset can be attributed to the $\sim 0\farcs42$ rms astrometric uncertainty (T. X. Thuan et al. 2004; C. Kehrig et al. 2018).

Nevertheless, the existence of an AGN remains questionable for the following reasons. First, Z. Peng et al. (2025) report a VB component ($v_{\mathrm{max}} \sim 5\,000$ km s^{-1}) in the forbidden [O III] λ5007 emission in SSCs 1&2. This finding is inconsistent with a Type 1 AGN interpretation, because the broad-line region (BLR) in such systems typically has electron densities of $n_e \gtrsim 10^8$ cm^{-3}, which would strongly collisionally de-excite the forbidden [O III] λ5007 emission. The observed v_{max} also exceeds those typically measured in local Type 2 AGNs ($\lesssim 2\,000$ km s^{-1}; e.g., N. L. Zakamska et al. 2003; C. M. Harrison et al. 2014; J.-H. Woo et al. 2016). Second, assuming the VB Hα component originates in the BLR, H26 estimate the BH mass to be $M_{\mathrm{BH}} \sim 10^6-10^8\,M_\odot$. This estimate exceeds the value predicted by the local black-hole-mass-stellar-mass ($M_{\mathrm{BH}}-M_*$) relation by $\sim 4-6$ dex (A. E. Reines & M. Volonteri 2015) at the stellar mass of SSCs 1&2 ($M_* \sim 10^6\,M_\odot$; A. E. Reines et al. 2008). Furthermore, it is $\gtrsim 2$ dex above the high-redshift $M_{\mathrm{BH}}-M_*$ relation derived for AGN and "little red dots" at $z \sim 2-9$ (F. Pacucci et al. 2023; K. Inayoshi & K. Ichikawa 2024; I. Juodžbalis et al. 2025).

Therefore, alternative physical mechanisms are required to account for the extreme broad wings, which are difficult to reconcile with an AGN framework.

Broad wings in strong emission lines can arise from galactic winds, in which the acceleration may be driven either by radiation pressure from central massive stars (e.g., N. Murray et al. 2005, 2011) or by the mechanical energy injected by core-collapse supernovae (CCSNe; e.g., T. A. Thompson et al. 2016; D. B. Fielding & G. L. Bryan 2022), although such models typically predict maximum velocities of $v_{\mathrm{max}} \lesssim (1-2)\times10^3$ km s^{-1}.

The observed broad wings may also arise from Thomson scattering at high column density, rather than from bulk Doppler motions. Such Thomson-scattering wings exhibit an exponential profile ($\propto e^{-|x|}$; K. Davidson 2020) and are frequently observed in the dense circumstellar medium (CSM) associated with Type IIn supernovae (SNe IIn; e.g., see references in R. A. Chevalier & C. Fransson 2017), which are characterized by strong shock interactions between the stellar/SN ejecta and a dense CSM. SNe IIn may originate from either genuine supernovae (e.g., N. N. Chugai 2001; C. Fransson et al. 2002) or supernova imposters (i.e., the star survives) like the giant eruption phase of η Carinae (e.g., K. Davidson et al. 1995; D. J. Hillier et al. 2001). Such giant eruptions are also often discussed in the context of super-Eddington outflows (e.g., E. Quataert et al. 2016). We note that although η Carinae is frequently cited as a luminous blue variable (LBV) in the literature, it is significantly more luminous than typical LBVs, which are usually called S Doradus-type variables (K. Davidson & R. M. Humphreys 2012; K. Davidson 2020).

Moreover, in η Carinae, the dense "Homunculus", a bipolar CSM formed primarily from the bulk ejecta of its giant eruption and responsible for the Thomson-scattering wings, absorbs most of the UV photons emitted by the luminous, hot star through dust and reradiates this energy in the infrared (K. Davidson et al. 2001; R. M. Humphreys & J. C. Martin 2012). The continuous shock interaction between the giant-eruption ejecta and the dense CSM powered sustained infrared thermal emission light curves that evolved slowly over $\sim 1840-1860$ (N. Smith et al. 2018). The Homunculus now exhibits a double-shell structure (e.g., K. Ishibashi et al. 2003), in which most of the mass ($\gtrsim 10\,M_\odot$) resides in a denser, geometrically thin outer shell traced by H_2 emission (hosting cold dust at ~ 140 K), while $\sim 10\%$ of the mass is contained in a geometrically thicker, inner shell of partially ionized gas traced by [Fe II] emission (hosting warm dust at ~ 200 K; e.g., K. Davidson & N. Smith 2000; N. Smith 2006).

In this work, we propose that an η Carinae-like giant eruption can naturally reproduce both the broad Hα wings and the NIR excess plateau observed in SSCs 1&2, motivated by their unusual spectral similarity to η

Table 1. Global Physical Properties of J0337−0502 Collected from the Literature

z	$\log(M_*)$ ($M_\odot$)	$\log(\mathrm{SFR})$ ($M_\odot\,\mathrm{yr}^{-1}$)	$\log(\mathrm{sSFR})$ (yr^{-1})	$\log(\dot{\Sigma}_*)$ ($M_\odot\,\mathrm{yr}^{-1}\,\mathrm{kpc}^{-2}$)	$12+\log(\mathrm{O/H})$	$E(B-V)$	$\log(L_{\rm bol})$ ($\mathrm{erg\,s}^{-1}$)	$R_{\rm core}$ (kpc)
0.01352	$7.06^{+0.24}_{-0.21}$	$-0.32^{+0.07}_{-0.11}$	$-7.37^{+0.26}_{-0.22}$	$-0.42^{+0.43}_{-0.84}$	7.46 ± 0.04	0.053 ± 0.006	43.08[a]	~ 1.40[b]

[a] This value is derived from the best-fit `CIGALE` SED model (H26) and is roughly consistent with the bolometric luminosity estimated from the total Hα emission of all SSCs (i.e., $L_{\rm bol}\sim(1-2)\times10^2\,L_{\rm H\alpha}\sim(4.5-9.0)\times10^{42}\,\mathrm{erg\,s}^{-1}$; R. C. Kennicutt & N. J. Evans 2012; D. Calzetti 2013), where the Hα luminosities of the individual SSCs are summarized in Table 2.

[b] This value refers to the radius of the high-SB "core" region, within which the Hα surface brightness drops rapidly from $\mathrm{SB_{H\alpha}}\sim2\times10^{-14}$ to $2\times10^{-16}\,\mathrm{erg\,s^{-1}\,cm^{-2}\,arcsec^{-2}}$ over the first 5″ (dominated by the central SSCs; E. C. Herenz et al. 2023a).

Note—Compiled from Tables 5 and 6 in D. A. Berg et al. (2022), Table A2 in X. Xu et al. (2022), and Section 4.1.1 in H26. For reference, the solar oxygen abundance is $12+\log(\mathrm{O/H})_\odot=8.69$ (M. Asplund et al. 2021).

Carinae. We also summarize the nebular properties of other SSCs for comparison (see Table 2 for key properties of each SSC compiled from the literature). Detailed analysis of the large-scale outflow kinematics and mass, momentum, and energy outflow rates will be presented in future work.

This work is organized as follows. In Section 2, we briefly summarize the configuration setup of our KCWI/KCRM observation of J0337-0502 and outline the essential steps employed to reduce the final mosaic cubes. We then derive the nebular properties of each SSC in Section 3, which are critical for inferring the potential signatures of giant eruption discussed in Section 4. In Section 5, we provide estimations of the CSM properties during the giant eruption phase, discuss the AGN possibilities, and assess the role of Lyα radiation pressure in SSCs 1&2. Finally, we summarize our results and the corresponding implications in Section 6. Throughout this work, we adopt the solar abundance for each element from M. Asplund et al. (2021) and assume a Flat ΛCDM cosmology with $\Omega_m=0.3$, $\Omega_\Lambda=0.7$, and $H_0=70$ km s^{-1} Mpc^{-1}.

2. OBSERVATION AND DATA REDUCTION

2.1. *KCWI/KCRM Observation*

We observed J0337-0502 on 2023 September 18 with the Keck Cosmic Web Imager (KCWI, the blue channel; P. Morrissey et al. 2018) and the Keck Cosmic Reionization Mapper (KCRM, the red channel) mounted on the Keck II telescope using the Small Slicer. The blue (red) channel was configured with the BL (RL) grating centered at 4600 Å (7700 Å), providing a usable spectral range of ∼ 3650 to 5550 Å (∼ 6200 to 9500 Å). The combination of narrow slits and the BL or RL grating resulted in an average spectral resolution of $R\sim3600$ for the blue channel and $R\sim2350$ for the red channel. The seeing determined from the FWHM of the point-spread function (PSF) of the standard star G191B2B was around 0.″9 in the blue channel and 0.″8 in the red channel. The airmass ranged from 1.17 to 1.21 during the observation.

We obtained exposures of 1320 s and 300 s for the blue channel and 4 × 300 s for the red channel at two pointings (shown in Figure 1). The initial exposure focused on the compact starburst, and then we offset approximately half the slicer width to the north, each subtending an 8.″4 × 20.″4 field of view (FoV). Since J0337-0502 exhibits spatially extended emissions (e.g., [O III] λ5007 and Hα) across the entire FoV, we chopped the slicer to a blank field and conducted off-field sky exposures of 660 s for the blue channel and 2 × 300 s for the red channel between the on-target exposures.

2.2. *Data Reduction*

We used the modified version of the KCWI Data Extraction and Reduction Pipeline (`KCWIDRP`; D. Neill et al. 2023) pipeline[7] for basic data processing, including overscan and bias subtraction, scattered-light subtraction, flat-fielding, geometric rectification, flux calibration, and corrections for differential atmospheric refraction. The default sky-subtraction stage of `KCWIDRP` generates a 2D model of the sky spectrum using b-splines, which are insufficient for wavelength regions densely populated with sky lines. Therefore, we skip this stage and instead employ a method based on principal component analysis (PCA) to improve sky subtraction (see below). We then leveraged the `KSkyWizard` package (Z. Zhuang et al., in prep.)[8] to iteratively improve the fitting of the inverse sensitivity curve and apply telluric correction of the red channel based on the `tellfit` function of `PypeIt` (J. X. Prochaska et al. 2020). Residuals be-

[7] https://github.com/yuguangchen1/KCWI_DRP/tree/KCWIKit

[8] https://github.com/zhuyunz/KSkyWizard

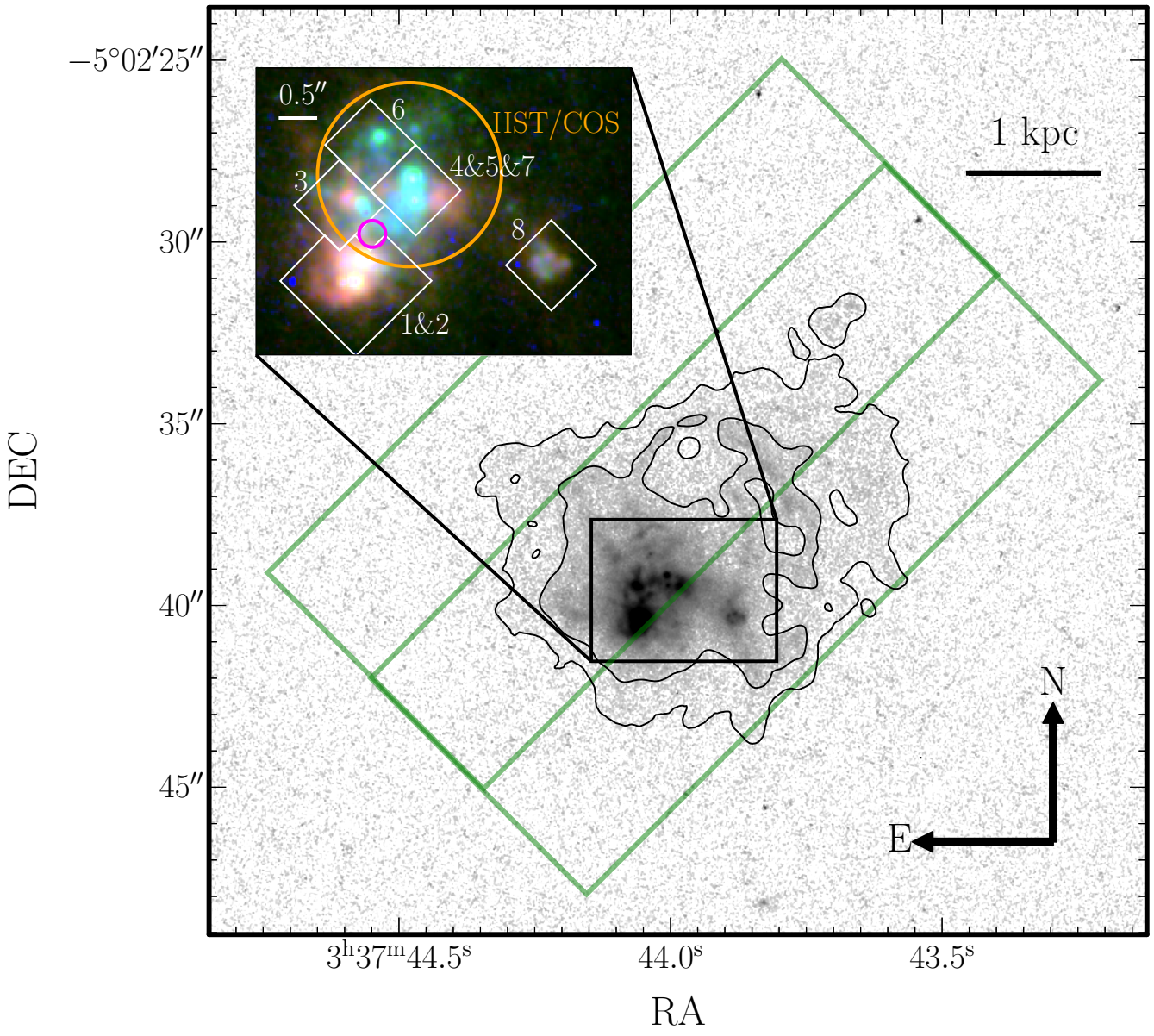


Figure 1. The two KCWI/KCRM observation pointings (green rectangles) are overlaid on the *HST* FR656N image of J0337-0502. The zoom-in panel shows the color-composite image (purple: F220W; blue: F330W; green: F435W; red: FR656N), which indicates the positions of the SSCs, including the luminous X-ray point source (magenta circle; T. X. Thuan et al. 2004), the apertures used to extract the 1D spectra, and the 2.″5 *HST*/COS circular aperture. The black solid contours demarcate Hα isophotes at $\mathrm{SB_{H\alpha}} \simeq \{2.5, 5.0\} \times 10^{-16}$ erg s^{-1} cm^{-2} arcsec^{-2}.

tween the flux-calibrated standard star spectra and the `KCWIDRP` reference spectra are within ±3%.

Based on the `LA Cosmic` (LAplacian Cosmic ray detection; P. G. van Dokkum 2001) algorithm, `KCWIDRP` utilizes the `astroscrappy` package (C. McCully et al. 2018) for cosmic-ray (CR) removal, which can efficiently identify CR-contaminated pixels in the blue channel where few sky lines are present. However, this edge detection algorithm, which uses the Laplacian kernel, incorrectly classifies most sky lines as CR in the red channel. For our science exposures with four consecutive frames, we could create the median frame and use sigma-clipping (3-sigma) to remove CR from these target frames. This sigma-clipping strategy does not apply to our sky exposures consisting of only two consecutive frames or to the standard star exposures taken during the 12- and 18-degree twilight, preventing us from computing the median frame accurately. Therefore, we trained a `Cosmic-CoNN` model (a deep-learning framework for cosmic ray detections designed for both spectroscopic and imaging data; C. Xu et al. 2023) on the KCRM datasets with at least three consecutive expo-

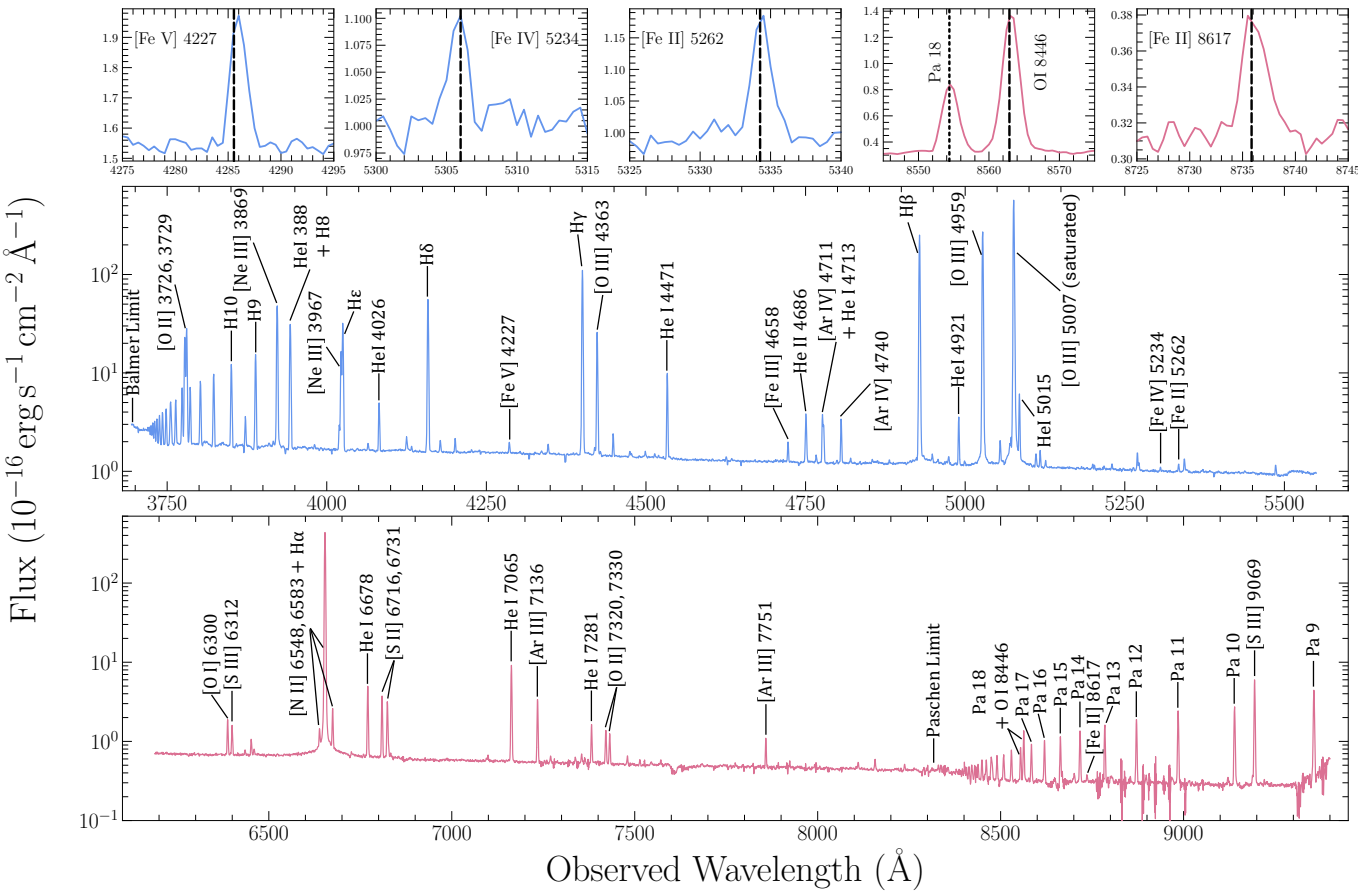


Figure 2. Extracted 1D spectra of KCWI (blue; second row) and KCRM (red; third row) for SSCs 1&2. First-row panels provide zoomed views around the detections of high-density gas indicators (Section 4.2), such as O I λ8446, [Fe II] λ5262, and [Fe II] λ8617, as well as the high and very-high ionization lines like [Fe IV] λ5234 and [Fe V] λ4227 (Section 3).

sures, which include both our observational data and the KCRM commissioning data (Peng et al. in prep.).

To improve sky subtraction, we utilize the modified version of the Zurich Atmosphere Purge (`ZAP`) package[9] (K. T. Soto et al. 2016). The GUI implementation of this modified ZAP version is available in `KSkyWizard` and discussed in Peng et al. (in prep.).

After subtracting the sky background from the reduced data cubes obtained from `KCWIDRP`, the cubes were aligned, stacked, and resampled into a mosaic cube with $0\farcs29\times0\farcs29\times0.5$ Å voxels using the `KCWIKIT`[10] package (N. Z. Prusinski & Y. Chen 2024; see Y. Chen et al. 2021 and N. Z. Prusinski et al. 2025 for additional details) with a drizzle factor of 1.0. Since Hγ, Hβ, and the [O III] $\lambda\lambda$4959, 5007 doublet are saturated in the regions around SSCs 1&2 for the 1320 s exposure frames of the blue channel (more than 60 000 counts in the raw 2D frames), we replaced these saturated pixels with corresponding pixels from the 300 s exposure frames. [O III] λ5007 is saturated in both 1320 s and 300 s exposures, so we only measure [O III] λ4959 for subsequent analysis and use the intrinsic ratio of the [O III] doublet (2.98; P. J. Storey & C. J. Zeippen 2000) to estimate the [O III] λ5007 flux.

To accurately locate each SSC within our reduced cubes, we aligned both the *HST* images (proposal ID 10575; PI: G. Östlin) and the KCRM narrow-band Hα image to the DECaLS r-band image (R. D. Blum et al. 2016; A. Dey et al. 2019). We then used the SSC apertures defined in Figure 1, which satisfy Nyquist sampling, to extract the corresponding 1D spectra from the data cubes (see Figure 2 for the spectra of SSCs 1&2).

3. NEBULAR PROPERTIES OF SSCS

In this section, we summarize the measured key nebular properties, including electron density and temperature (n_e, T_e), ionization parameter ($\log U$), and gas-phase abundances (oxygen, nitrogen, and iron), for all SSCs shown in Figure 1. The methods used to derive these nebular properties are described in Appendix A in detail. We then combine these measurements (summarized in Table 3) with other observed nebular properties

[9] https://github.com/jasonpeng17/zap_for_kcwi
[10] https://github.com/yuguangchen1/KcwiKit

Table 2. Physical Properties of each SSC in J0337-0502 Collected from the Literature

Region	Age	Stellar Mass	$R_{\rm H\,II}$	$L_{\rm H\alpha}$
	(Myr)	($M_\odot$)	(pc)	(10^{38} erg s^{-1})
SSC 1	3.0	4.7×10^5	11 ± 11	207 ± 2
SSC 2	3.0	3.7×10^5	10 ± 10	134 ± 1
SSC 3	7.0	7.1×10^5	29 ± 27	23.2 ± 0.6
SSC 4	11.0	1.1×10^6	33 ± 27	9.7 ± 0.4
SSC 5	13.0	2.9×10^6	39 ± 30	9.2 ± 0.4
SSC 6	11.0	2.6×10^5	21 ± 21	2.6 ± 0.2
SSC 7	4.0	9.4×10^4	15 ± 10	42 ± 4
SSC 8	8.0	2.2×10^5	21 ± 10	13 ± 1

NOTE—Age, stellar mass, H II region Strömgren radius ($R_{\rm H\,II}$), and Hα luminosity ($L_{\rm H\alpha}$, assuming a luminosity distance of 58 Mpc) for each SSC available in the literature (R. I. Thompson et al. 2009; A. Adamo et al. 2010). The Strömgren radius of SSC 7 and SSC 8 are derived using $R_{\rm H\,II} = \left(3\,Q_{\rm LyC}/4\,\pi\,n_{\rm H}^2\,\alpha_B\,f\right)^{1/3}$. Consistent with A. Adamo et al. (2010), we derive $Q_{\rm LyC}$ from the `STARBURST99` $Z = 0.0004$ model (C. Leitherer et al. 1999), assume a gas filling factor of $f = 0.01$, and adopt the Case B recombination coefficient α_B at 20 000 K. Similar to A. Adamo et al. (2010), $n_{\rm H}$ of SSC 7 (SSC 8) is assumed to range from 10^3 to 10^4 cm^{-3} (5×10^2 to 10^3 cm^{-3}). The $L_{\rm H\alpha}$ of SSC 7 and SSC 8 are converted from their Paα luminosities (R. I. Thompson et al. 2009) using the Case B recombination ratio (i.e., Hα/Pa$\alpha \simeq 9.15 - 9.72$ for $T_e \in [15\,000, 20\,000]$ K and $n_e \in [10, 5\,000]$ cm^{-3}; V. Luridiana et al. 2013).

from the literature to highlight the distinguishing nebular characteristics of SSCs 1&2 compared to other SSCs in Section 4.

Line ratios are key constraints for deriving the nebular properties in our analysis. We employ the `Python` package `VerEmisFitting` (Z. Peng & Y. Li 2024; Z. Peng et al. 2025) to model each emission line's profile. Both single-Gaussian and multi-component models are utilized–for example, a double-Gaussian plus Lorentzian (dGL) model for Hα as shown in Section 4.5–to fit the observed line profiles. It is noteworthy that the observed broad-wing line profile of Hα cannot be well described by a Lorentzian model (i.e., $\propto x^{-2}$), but is instead better characterized by the wings of a Thomson-scattering profile (i.e., $\propto e^{-|x|}$). This is a key signature of an optically thick outflow produced by a giant eruption, such as that observed in η Carinae, and more generally by SNe IIn (see Section 4.5 for details; K. Davidson et al. 1995; N. N. Chugai 2001; D. J. Hillier et al. 2001; L. Dessart et al. 2009; R. M. Humphreys et al. 2012; A. Mehner et al. 2015; K. Davidson 2020).

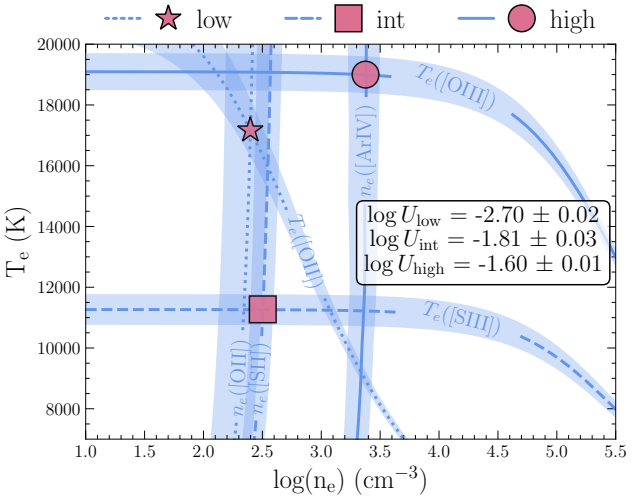


Figure 3. T_e and n_e solutions for SSCs 1&2. The best-fit T_e and n_e for each ionization zone are defined as the intersection of the temperature and density diagnostics. The estimated log U value for each ionization zone is also shown in the panel.

3.1. n_e, T_e, and log U Constraints of Different Ionization Zones

We characterize the physical conditions of the ionized gas by separating the nebulae into multiple ionization zones following D. A. Berg et al. (2021, hereafter B21; see Appendices A.2 and A.3 for the diagnostics used to define each ionization zone). This approach should be regarded as a simplified parameterization of an intrinsically clumpy and multiphase nebular medium, because each "zone" may in reality comprise a collection of gas condensations with a wide range of physical conditions.

Figure 3 shows the derived T_e, n_e, and log U values using `PyNeb` for the low (14.5 – 20.6 eV), intermediate (23.3 – 34.8 eV), and high (35.1 – 54.9 eV) ionization zones for SSCs 1&2 (see Appendix A for other SSCs). T_e within the high-ionization zone reaches T_e([O III]) = 19 000 ± 600 K, while lower-ionization zones show cooler gas, with T_e([S III]) = 11 000 ± 500 K and T_e([O II]) = 17 200 ± 1600 K. n_e inferred from low-ionization diagnostics are modest, with n_e([S II]) = 320 ± 70 cm^{-3} and n_e([O II]) = 250 ± 100 cm^{-3}, whereas the high- to very-high (VH; > 54 eV) ionization gas traced by [Ar IV] indicates systematically denser gas, with n_e([Ar IV]) = 2 400 ± 700 cm^{-3}. The estimated log U values for the low-to-intermediate ("low"; [S III]/[S II]), intermediate-to-high ("int"; [O III]/[O II]), and high-to-VH ("high"; [Ar IV]/[Ar III]) ionization zones span −2.70 to −1.60.

Table 3. SpectroscopicallyDerived Nebular Properties of SSCs

Property	Zone	SSCs 1&2	SSC 3	SSCs 4&5&7	SSC 6	SSC 8
T_e([Fe V])$_{\rm CL}$ (K)	VH	$\sim 23\,000$	···	···	···	···
T_e([O III]) (K)	H	$19\,000 \pm 600$	$18\,200 \pm 170$	$19\,500 \pm 200$	$18\,400 \pm 180$	$18\,300 \pm 380$
T_e([S III]) (K)	I	$11\,000 \pm 500$	$15\,900 \pm 330$	$15\,800 \pm 610$	$19\,400 \pm 690$	$1\,5200 \pm 2\,200$
T_e([O II]) (K)	L	$17\,200 \pm 1\,600$	$16\,100 \pm 2\,700$	$15\,700 \pm 3\,800$	$15\,700 \pm 5\,000$	$1\,3000 \pm 3\,900$
T_e([Fe II])$_{\rm CL}$ (K)	PI	$\sim 7\,500$	···	···	···	···
n_e([Ar IV]) (cm^{-3})	VH	$2\,400 \pm 700$	$2\,200 \pm 420$	$2\,800 \pm 950$	$2\,600 \pm 870$	$4\,100 \pm 2\,900$
n_e([S II]) (cm^{-3})	L	320 ± 70	180 ± 50	150 ± 70	250 ± 90	10 ± 10
n_e([O II]) (cm^{-3})	L	250 ± 100	180 ± 20	140 ± 30	90 ± 90	80 ± 20
n_e([Fe II]) (cm^{-3})	PI	$\sim 10^6$	$\sim 10^6$	···	···	···
$\log U_{\rm low}$ ([S III]/[S II])	I/L	-2.70 ± 0.02	-2.61 ± 0.01	-2.52 ± 0.01	-2.55 ± 0.01	-2.79 ± 0.01
$\log U_{\rm int}$ ([O III]/[O II])	H/I	-1.81 ± 0.03	-1.77 ± 0.01	-1.71 ± 0.01	-1.71 ± 0.01	-2.02 ± 0.01
$\log U_{\rm high}$ ([Ar IV]/[Ar III])	VH/H	-1.60 ± 0.01	-1.60 ± 0.01	-1.52 ± 0.02	-1.58 ± 0.01	-1.90 ± 0.03
$\log U_{\rm ave}$	L/I/H	-1.67 ± 0.01	-1.67 ± 0.01	-1.59 ± 0.02	-1.64 ± 0.01	-2.08 ± 0.03
12 + log(O/H)	All	7.32 ± 0.02	7.38 ± 0.01	7.30 ± 0.01	7.38 ± 0.06	7.21 ± 0.01
12 + log(N/H) (B21)	All	6.30 ± 0.02	6.20 ± 0.02	6.21 ± 0.02	6.13 ± 0.07	6.10 ± 0.03
12 + log(N/H) (M. Peimbert & R. Costero 1969)	All	6.02 ± 0.03	5.91 ± 0.02	5.82 ± 0.02	5.86 ± 0.07	5.67 ± 0.03
12 + log(N/H) (C. Esteban et al. 2020)	All	6.11 ± 0.03	6.00 ± 0.02	5.90 ± 0.02	5.94 ± 0.07	5.78 ± 0.03
12 + log(Fe/H)	All	5.81 ± 0.06	···	···	···	···
12 + log(Fe/H) (B21)	All	6.02 ± 0.03	6.03 ± 0.02	6.20 ± 0.04	6.01 ± 0.08	5.93 ± 0.05
log(N/O) (B21)	All	-1.02 ± 0.02	-1.17 ± 0.01	-1.09 ± 0.02	-1.25 ± 0.03	-1.11 ± 0.03
log(N/O) (M. Peimbert & R. Costero 1969)	All	-1.29 ± 0.02	-1.46 ± 0.01	-1.48 ± 0.02	-1.52 ± 0.03	-1.54 ± 0.03
log(N/O) (C. Esteban et al. 2020)	All	-1.21 ± 0.02	-1.38 ± 0.01	-1.39 ± 0.02	-1.43 ± 0.03	-1.44 ± 0.03
log(Fe/O)	All	-1.52 ± 0.06	···	···	···	···
log(Fe/O) (B21)	All	-1.30 ± 0.03	-1.34 ± 0.02	-1.10 ± 0.04	-1.37 ± 0.04	-1.28 ± 0.05
$E(B-V)_{\rm int}$	All	0.06 ± 0.01	0	0	0	0

Note—Electron temperatures, densities, $\log U$, element abundances, and intrinsic color excesses for the SSCs in J0337-0502, derived using the methodologies described in Section 3.1 and Appendix A. Column 2 specifies each property's ionization zone(s), where PI = partially ionized, L = low, I = intermediate, H = high, VH = very high, and All = all ionization zones.

Moreover, a key result of this work is the identification of an extremely dense partially ionized (PI) zone ($\sim 8-15$ eV), traced by [Fe II] emission, in SSCs 1&2. Figure 4 compares the observed [Fe II] λ5262/[Fe II] λ8617 ratios for SSCs 1&2 and SSC 3 with theoretical predictions computed at various n_e and T_e values using `PyNeb` (V. Luridiana et al. 2015). SSCs 1&2 are the only clusters that have $> 3\sigma$ detections in both [Fe II] lines. SSC 3 only has a $\sim 2.3\sigma$ ($\sim 2.8\sigma$) detection for [Fe II] λ5262 ([Fe II] λ8617). At T_e ranges from 5 000 to 12 500 K, we constrain $10^6 \lesssim n_e \lesssim 10^7$ cm^{-3} for both SSCs 1&2 and SSC 3 in the PI region (compare to the densities inferred for gas traced by [Fe II] and [Fe III] in the "Weigelt knots" of η Carinae; A. Mehner et al. 2010; F. Hamann 2012, see Figure 4]). If we use the ion-fraction-weighted temperature of [Fe II] from the best-fitting `CLOUDY` models (see Section 4.2 for details) to estimate T_e ([Fe II])$_{\rm CL}$ (e.g., $\sim$ 7 500 K for SSCs 1&2) in the PI zone, the lower end of this n_e constraint is favored (i.e., $n_e \sim 10^6$ cm^{-3}). Based on their higher [Fe II] λ5262/[Fe II] λ8617 ratio, SSCs 1&2 are ~ 0.2 dex denser than SSC 3 within the PI zone, but remain consistent with SSC 3 within 1σ.

Notably, although n_e in the neutral zone cannot be directly constrained, the detection of O I λ8446 in all SSCs, the Bowen Resonance Fluorescence line of Lyβ, suggests an optically-thick region where Lyα trapping can effectively pump the $n = 2$ level in neutral hydrogen gas. The O I λ8446/Hα ratio can therefore serve as a tracer of optical depth (e.g., H. Netzer & M. V. Penston 1976; S. Johansson & V. S. Letokhov 2005). We find that O I λ8446/Hα reaches its highest value in SSCs 1&2 ($\sim 2.5 \times 10^{-3}$), followed by SSC 3 and SSC 8 ($\sim 1.8 - 2.0 \times 10^{-3}$), and decreases further in SSCs 4 to 7 ($\sim 1.2 - 1.3 \times 10^{-3}$). This trend is consistent with the high-density sequence independently inferred from the [Fe II] diagnostics, and also with the increasing stellar population age listed in Table 2. In this picture, radiative and mechanical feedback from massive stars can progressively disperses the dense neutral gas within the SSCs. We therefore use the O I λ8446/Hα ratio to estimate $\tau_{\rm Ly\alpha}$ (and the corresponding hydrogen column density $N_{\rm H}$) and examine the spatial correspondence between O I and [Fe II] emission in Section 4.2.

3.2. *Gas-phase Abundances of N, O, and Fe*

To determine the gas-phase ionic abundances of N, O, and Fe, we adopt the corresponding T_e and n_e measurements for each ionization zone described in Section 3.1. The specific emission lines and ionization correction factors (ICFs) used to derive each abundance are summarized in Appendix A.4.

We consider the first two ionization stages of oxygen (O^+ and O^{+2}) to derive the oxygen abundance. The derived oxygen abundance expressed as 12 + log(O/H) ranges from 7.21 ± 0.01 for SSC 8 to 7.38 ± 0.06 for SSC 6. Notably, the oxygen abundance for SSC 6 is measured for the first time in this work, while the measurements

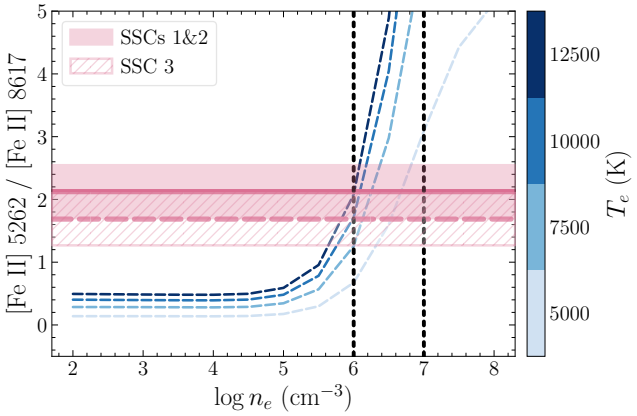


Figure 4. The [Fe II] λ5262/[Fe II] λ8617 ratio for SSCs 1&2 (solid red) and SSC 3 (dashed red). Predictions of the [Fe II] λ5262/[Fe II] λ8617 ratio across different n_e and T_e are shown as dashed bluish lines. The rough n_e constraints for gas traced by [Fe II] and [Fe III] in the Weigelt knots of η Carinae are shown as dotted lines.

for the other SSCs are consistent with previous studies (e.g., T. X. Thuan et al. 2004; P. Papaderos et al. 2006; Y. I. Izotov et al. 2009).

For nitrogen, we consider only the first ionization stage (N^+) and apply three different ICF(N^+) to estimate the nitrogen abundance. We find that SSCs 1&2 exhibit a log(N/O) value that is $\sim 0.1 - 0.2$ dex higher than those of other SSCs, regardless of the choice of ICF(N^+). We account for systematic uncertainties in ICF(N^+), which can vary log(N/O) by up to 0.3 dex, when comparing SSCs 1&2 to other high-log(N/O) galaxies in the literature in Section 4.4. We also note that although Y. I. Izotov et al. (2009) adopt an ICF(N^+) that is a function of $O^+/(O^+ + O^{2+})$, as in M. Peimbert & R. Costero 1969 and C. Esteban et al. 2020, their derived log(N/O) for SSCs 1&2 is $\sim 0.1-0.2$ dex lower than those obtained using the latter ICF prescriptions.

Because we detect Fe at $> 3\sigma$ significance in multiple ionization states—Fe^+ (PI), Fe^{+2} (low-intermediate), Fe^{+3} (intermediate-high), and Fe^{+4} (VH)—we include all four stages when determining the gas-phase iron abundance in SSCs 1&2. This approach is not applicable to the other SSCs: for SSCs 3 to 7 we adopt ICF(Fe^{+2}+Fe^{+4}), while for SSC 8 we use ICF(Fe^{+2}). The derived log(Fe/O) value for SSCs 1&2 is $\sim 0.1-0.3$ dex lower than those of other SSCs. However, this comparison is subject to systematic uncertainties in the adopted Fe ICFs. For example, if we instead adopt the B21 ICF(Fe^{+2}+Fe^{+4}) for SSCs 1&2, we find that the log(Fe/O) of SSCs 1&2 is comparable to those of SSCs 3, 6, and 8 (see Table 3).

4. SIGNATURES OF GIANT ERUPTION IN SSCS 1&2

As summarized in Section 3, SSCs 1&2 are distinct from the other SSCs in that they are the only clusters exhibiting: (1) $> 3\sigma$ detections of [Fe II] emission lines, implying $n_e \sim 10^6$ cm^{-3} in the PI zone (see Sections 4.2 and 4.3 for the stellar and nebular conditions required to produce the observed [Fe II] emission); and (2) nitrogen enrichment relative to the remaining SSCs (see Section 4.4 for the possible origin). When combined with their detections of warm dust (L. K. Hunt et al. 2014), radio emission (K. E. Johnson et al. 2009), H_2 emission (R. I. Thompson et al. 2009), and Thomson-scattering broad wings (Section 4.5), these characteristics strongly motivate a detailed investigation of the underlying source of excitation in SSCs 1&2.

Since these spectral features are also observed in η Carinae (e.g., K. Davidson et al. 1982, 1986; R. A. Duncan et al. 1995; D. J. Hillier et al. 2001; K. Davidson & R. M. Humphreys 2012; K. Davidson 2020), we propose that these unusual features in SSCs 1&2 arise during an η Carinae-like giant-eruption phase. We calibrate the relevant physical mechanisms using the exceptionally well-studied giant eruption of η Carinae as a reference case.

In this section, we first present a coherent physical picture based on an η Carinae-like giant eruption that can naturally account for the unusual spectral features observed in SSCs 1&2 (Section 4.1). We then provide detailed analyses of each key feature in Sections 4.2 through 4.5 (and also in Section 5.1).

4.1. *A Coherent Giant Eruption Picture*

During the giant eruption phase (starting ~ 5 years ago based on the NIR variability; H26), the shock interaction between the giant eruption ejecta (CNO-cycled material) and the surrounding CSM formed by pre-eruption stellar winds results in a typical forward shock/reverse shock structure (see Figure 5; K. Davidson & R. M. Humphreys 2012; N. Smith 2017a; R. A. Chevalier & C. Fransson 2017). At the contact discontinuity, a Rayleigh-Taylor-unstable cold dense shell (CDS) forms; this CDS is optically thick to UV radiation and likely hosts cold dust (~ 80 K; M. Mingozzi et al. 2025) and H_2 emission (R. I. Thompson et al. 2009). Most of the outgoing flux from the reverse shock is absorbed by the CDS. The region downstream of the reverse shock (with $n_e \sim 10^6\,\mathrm{cm}^{-3}$ and $T_e \sim 7 \times 10^3$ K; Section 3.1), partially photoionized by the primary cool star ($T_{\rm eff} \sim 1.5 \times 10^4$ K), is the source of the observed [Fe II] emission (Section 4.3). This same region efficiently converts kinetic energy into radiation, cools the gas, and drives efficient warm-dust formation ($\sim 400-500$ K), thereby producing the NIR excess emission (Section 4.2). In contrast, radiative cooling in the forward shock explains both the luminosities of very-high-ionization lines such as [Fe V] λ4227 and luminous X-ray point source (Section 5.1). Furthermore, Thomson scattering within the pre-shock CSM causes a red-excess asymmetry in the Hα line profile, with blue and red wings extending to velocities of $-5\,000$ km s^{-1} and $10\,000$ km s^{-1}, respectively (Section 4.5). The following sections provide a detailed illustration of each observed signature summarized above.

4.2. *High-Density Gas*

The detections of the [Fe II] lines (Figures 2 and 4) reveal the high-density PI region found in SSCs 1&2. Moreover, the detection of Lyβ-pumped O I λ8446 also suggests an optically-thick neutral region where Lyα trapping is efficient. O I λ8446 is also observed in the Weigelt knots of η Carinae (S. Johansson & V. S. Letokhov 2005).

This high-density region might arise from the shock interaction between the giant eruption ejecta and the pre-eruption stellar wind material that forms the dense CSM. If the observed warm dust (e.g., L. K. Hunt et al. 2014) forms in this same region, we can use the photoionization model `CLOUDY` (v23.01; M. Chatzikos et al. 2023) to estimate the stellar and nebular conditions required to reproduce the observed dust temperature and the corresponding NIR excess. We vary the blackbody (BB) effective temperature, $T_{\rm eff}$, from 8×10^3 to 4.3×10^4 K, the total luminosity ($L_{\rm tot}$) from 10^{39} to 10^{40} erg s^{-1} (based on the S Dor instability strip on the HR diagram; B. Wolf 1989; R. M. Humphreys & K. Davidson 1994; K. Weis & D. J. Bomans 2020), the hydrogen density, $n_{\rm H}$, from 10^6 to 10^7 cm^{-3} (constraints derived from the [Fe II] ratio), and the inner radius, $r_{\rm in}$ (from the central ionizing source to the illuminated face of the cloud), at 10^{16}, 10^{17}, and 10^{18} cm.

Figure 6 shows that the `CLOUDY` model with $T_{\rm eff} = 1.5 \times 10^4$ K, $\log U \sim -2$, $n_{\rm H} = 10^6$ cm^{-3}, and $r_{\rm in} = 10^{16}$ cm best reproduce the warm-dust temperature ($T_{\rm dust} \sim 400 - 500$ K) and the observed NIR excess in the W1 and W2 bands. Here, $T_{\rm dust}$ is constrained by fitting a `DUSTY` model (Z. Ivezic & M. Elitzur 1997), which analytically solves the radiative transfer of a spherical dust shell heated by a stellar point source, in L. K. Hunt et al. (2014) and the derived $W1-W2$ color temperature in H26. This result holds when adopting a CNO-cycle chemical composition (A. Mehner et al. 2010).

The `CLOUDY` model best matching the observed O I λ8446/Hα ratio has $\tau_{\rm Ly\alpha} \sim 10^8$, supporting the existence of high-density neutral gas within SSCs 1&2. This inferred $\tau_{\rm Ly\alpha}$ corresponds to a hydrogen column density of $\log(N_{\rm H}/\mathrm{cm}^{-2}) \sim 22$, since $\tau_{\rm Ly\alpha} \sim \sigma_{\rm Ly\alpha} N_{\rm H} \sim (1.5 - 7.5) \times 10^8$ for Doppler broadening parameters in the range $b = 10-50\,\mathrm{km\,s}^{-1}$. Notably, this column density is consistent with that inferred from the [Fe II] diagnostics and best-fit `CLOUDY` model (i.e., $N_{\rm H} \sim n_{\rm H}\, r_{\rm in} \sim (10^6\,\mathrm{cm}^{-3})\,(10^{16}\,\mathrm{cm}) \sim 10^{22}\,\mathrm{cm}^{-2}$). The agreement between the column densities independently inferred from O I and [Fe II] emission suggests that both lines likely

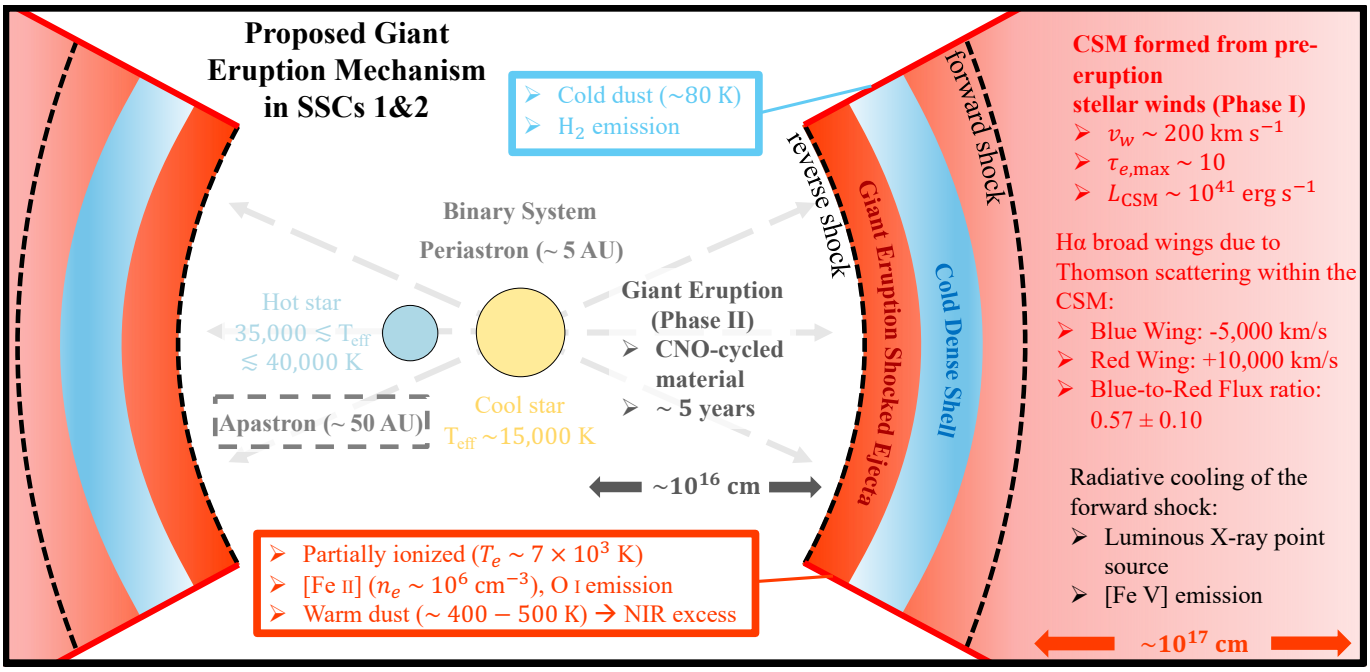


Figure 5. Illustration of the proposed giant eruption mechanism (adapted from the η Carinae picture; e.g., A. Mehner 2011; K. Davidson 2020; T. R. Gull et al. 2022) in SSCs 1&2. The high-density CSM initially forms from pre-eruption stellar winds (Phase I). Subsequent shock interaction between the giant eruption ejecta (Phase II; near periastron if the system is binary) and the CSM naturally accounts for the observed spectroscopic signatures discussed in Section 4. We illustrate the proposed picture in Section 4.1.

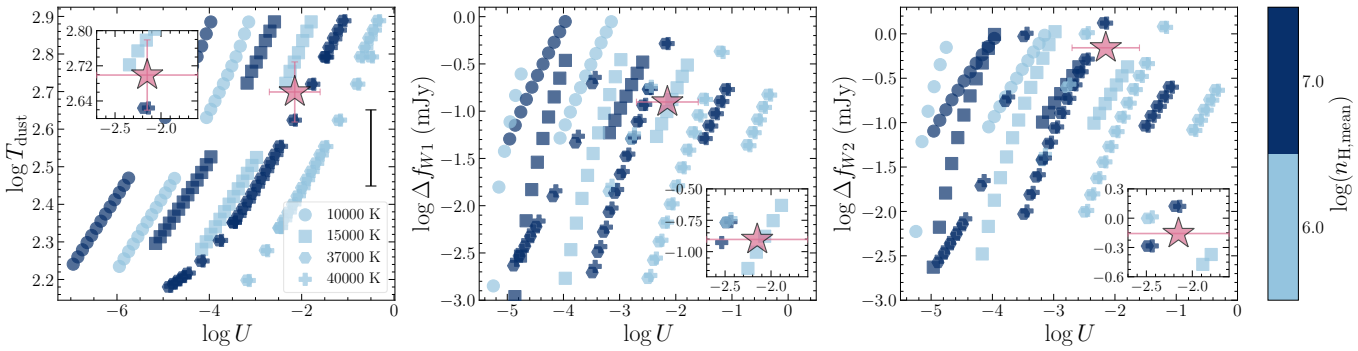


Figure 6. *Left:* CLOUDY predictions of the innermost dust temperature, $T_{\rm dust}$. The typical 1σ radial scatter in dust temperature across grain species is indicated in the panel. *Middle:* The predicted near-infrared (NIR) excess in the W1 band ($\Delta f_{\rm W1}$). *Right:* The predicted NIR excess in the W2 band ($\Delta f_{\rm W2}$). These predictions are compared with the observational constraints on $T_{\rm dust}$ from L. K. Hunt et al. (2014) and H26, and the measured $\Delta f_{\rm W1}$ and $\Delta f_{\rm W2}$ from H26. The displayed $\log U$ of our observation (red star) represents the ionization-weighted value from the low- to high-ionization zones (Section 3).

originate from the same high-density region (see Figure 5).

4.3. *Low and High Ionization Fe Lines*

The simultaneous detection of iron in ionization stages from Fe^{+} to Fe^{+4} in SSCs 1&2 is rarely seen in other low-metallicity star-forming galaxies (e.g., B21). Such detections require not only the presence of hard ionizing photons with energies $\gtrsim$ 55 eV to produce [Fe V] emission, but also extremely dense gas capable of self-shielding against these photons to preserve [Fe II] emission.

To gain more insights into the excitation mechanism of each ionization stage of iron, we compare the observed Fe line ratios ([Fe III] λ4658 (left), [Fe IV] λ5234 (middle), and [Fe V] λ4227 (right), relative to [Fe II] λ5262 plus [Fe II] λ8617) with CLOUDY model predictions (Figure 7). We find that the relatively low-ionization ratio ([Fe III]/[Fe II]) is consistent with a photoionization solution for a cool star ($T_{\rm eff}$ = 14 000 K and

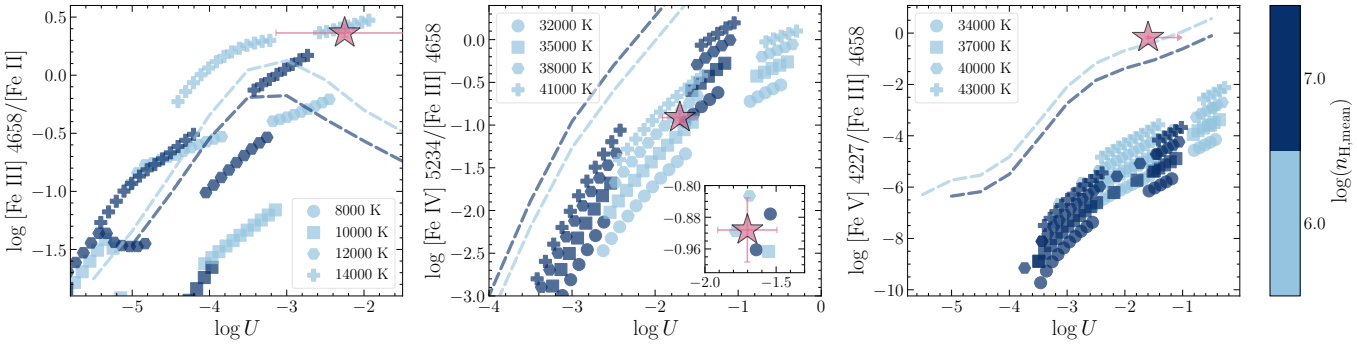


Figure 7. Comparison of observed (red star) Fe line ratios–the combined [Fe II] emission ([Fe II] λ5262 plus [Fe II] λ8617) (left), [Fe IV] λ5234 (middle), and [Fe V] λ4227 (right)–relative to [Fe III] λ4658. Overplotted are `CLOUDY` model predictions (color-coded by $n_{\rm H}$ and shaped by input blackbody $T_{\rm eff}$) and AGN model curves (dashed lines with the same color coding).

$L_{\rm tot}/L_\odot = 10^{5.70\pm0.20}$). In contrast, a high $T_{\rm eff}$ solution ($T_{\rm eff} \sim 3.5-4.0\times10^4$ K and $L_{\rm tot}/L_\odot = 10^{6.20\pm0.40}$) at $n_{\rm H} = 10^6$ cm^{-3} (the preferred $n_{\rm H}$ in Figure 6) can potentially reproduce the [Fe IV]/[Fe III] ratio. The inferred $T_{\rm eff}$ for the low and high ionization lines are similar to those of η Carinae which exists in a binary system (A. Mehner et al. 2010; K. Davidson 2012). However, even the hottest models ($T_{\rm eff} = 4.3\times10^4$ K) underpredict the observed [Fe V]/[Fe III] ratio by $3-4$ orders of magnitude.

To explore whether AGN photoionizes the high ionization lines (see details in Appendix B), we run a set of AGN models through `CLOUDY` based on the nebular properties of SSCs 1&2, shown as dashed lines in Figure 7. These AGN models underestimate the [Fe III]/[Fe II] and overestimate the [Fe IV]/[Fe III] ratios, but can potentially reproduce the observed [Fe V]/[Fe III] ratio. However, the AGN models that can potentially reproduce the [Fe V]/[Fe III] ratio have $n_{\rm H} = 10^6$ cm^{-3}, which is comparable to the critical density of [Fe V] λ4227, where collisional de-excitation becomes significant. Consequently, the predicted [Fe V] line luminosity is substantially lower than observed; specifically, the modeled [Fe V] λ4227/Hβ ratio ($\sim 10^{-4}$) is approximately a dex smaller than the observed value ($\sim 10^{-3}$). We propose that this VH-ionization line arise from the radiative cooling of the CSM shock interaction (see Section 5).

To further explore the excitation mechanisms for these iron lines, we also present the temporal evolution of their line ratios for SSCs 1&2 over the past $\sim$ 20 years in Figure 8. The [Fe II]/[Fe III] (solid) and [Fe V]/[Fe III] (dotted) ratios remain consistent within 1σ over $\sim$20 years. However, the [Fe IV] (dashed) detection in the VLT/MUSE spectrum (MJD 57342; E. C. Herenz et al. 2023a,b) is below 3σ (and is not reported for VLT/FORS; E. C. Herenz et al. 2023a,b), so we only derive upper limits. The tentative variability of [Fe IV] (i.e., increases by a factor of $\gtrsim 2$ over the past eight years) can be qualitatively explained if the giant-eruption candidate in SSCs 1&2 exists in a binary system analogous to η Carinae (e.g., references in K. Davidson & R. M. Humphreys 2012). In this scenario, the secondary hot star ($T_{\rm eff} \sim 3.5-4.0\times10^4$ K) should provide the ionizing photons responsible for the [Fe IV] emission, while the primary cool star ($T_{\rm eff} \sim 1.5\times10^4$ K), having recently undergone eruptions, sustains the [Fe II] emission. During the binary system's periastron (roughly when the proposed giant eruption phase starts), the ionizing UV radiation from the secondary star is temporarily suppressed as it plunges into the primary's dense wind, leading to a significant decline in the [Fe IV] luminosity.

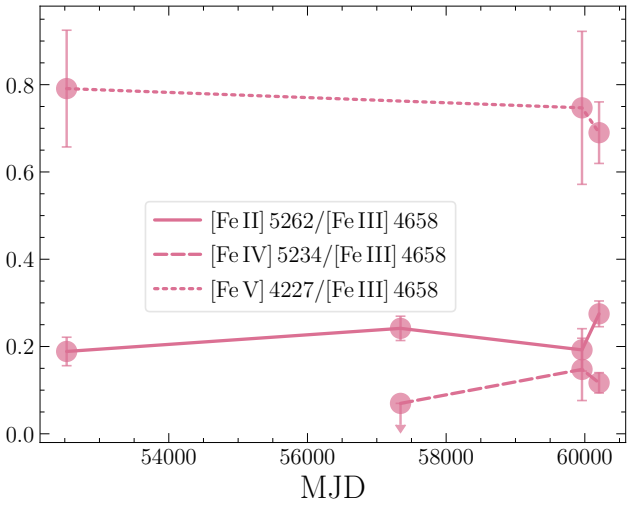


Figure 8. Temporal evolution of forbidden Fe line ratios–[Fe II]/[Fe III] (solid), [Fe IV]/[Fe III] (dashed), and [Fe V]/[Fe III] (dotted)–based on VLT/FORS (MJD 52527; Y. I. Izotov et al. 2009), VLT/MUSE (MJD 57342; E. C. Herenz et al. 2023a,b), Keck/ESI (MJD 59959; Z. Peng et al. 2025), and our KCWI/KCRM data (MJD 60205; this work).

Nevertheless, we emphasize that a binary system has not been shown to be strictly necessary for an η Carinae-like giant eruption (e.g., K. Davidson 2020). Hence,

higher-cadence observations will be necessary to confirm any periodic variability in [Fe IV] and to distinguish it from enhanced emission driven by radiative cooling in the proposed CSM interaction during the giant-eruption phase (i.e., non-periodic; see Section 5.1.2 for details).

4.4. *Nitrogen and Iron Abundances: Comparison with Literature Values*

4.4.1. N/O *Abundance Ratio*

We find that the N/O abundance ratio in SSCs 1&2, $\log(\mathrm{N/O}) \sim -1.30$ to -1.0 (accounting for systematic ICF(N^+) uncertainties; Section 3.2), is approximately $0.2-0.5$ dex higher than that of typical local H II regions (L. S. Pilyugin et al. 2012) at the extreme low-metallicity end ($12+\log(\mathrm{O/H}) \lesssim 7.5$) in the N/O-O/H diagram (left panel of Figure 9), where previous studies have reported a "tight plateau" ($\log(\mathrm{N/O})_{\rm plat} \sim -1.6$ to -1.4) at this end (e.g., Y. I. Izotov & T. X. Thuan 1999; A. Nava et al. 2006).

This observed high N/O ratio is more extreme when compared with known local metal-poor dwarf galaxies with mild nitrogen enrichments ($\log \mathrm{N/O} - \log(\mathrm{N/O})_{\rm plat} \lesssim 0.1$), such as Region-3 (Reg-3) of DDO 68 (F. Annibali et al. 2019), Leo P (E. D. Skillman et al. 2013), and targets like J1044+0353 presented in D. A. Berg et al. (2019). The broad-emission component of Mrk 996 ($z = 0.0054$) is the sole exception, where a similar nitrogen enrichment is observed in a relatively metal-rich environment ($12+\log(\mathrm{O/H}) \sim 8.3$; B. L. James et al. 2009).

Nitrogen enhancements are more commonly observed in high-redshift galaxies, e.g., Godzilla of the Sunburst Arc ($z \sim 2.4$; M. Pascale & L. Dai 2024), several $z \sim 5$ (K. Z. Arellano-Córdova et al. 2024) and $z \sim 6$ (H. Yanagisawa et al. 2024) galaxies observed by JWST, and GN-z11 ($z \sim 10.6$; P. Senchyna et al. 2024). Among the high N/O targets, potential giant eruption and/or LBV candidates have been identified in Reg-3 of DDO 68 (Y. I. Izotov & T. X. Thuan 1999) and Godzilla (S. Choe et al. 2025). S. Choe et al. (2025) also qualitatively claim that the giant-eruption candidate Godzilla likely has a hotter companion star, a scenario we propose for SSCs 1&2 in Section 4.3.

The conventional primary and secondary production channels of nitrogen cannot explain the large scatter of N/O values observed at the low-metallicity end (e.g., B. M. Tinsley 1980; B. E. J. Pagel 2009), which suggests the need for earlier nitrogen enrichment prior to the onset of CCSNe from massive stars (i.e., $\lesssim 3$ Myr). For example, an explanation based on the ejection of nitrogen-rich material during the Wolf-Rayet (WR) phase (typically $\sim 3-6$ Myr) cannot reproduce such high N/O ratios at these early times given the extremely young stellar populations of SSCs 1&2 (~ 3 Myr; see Table 2); additionally, the characteristic broad helium emission lines and WR bumps associated with WR winds are not observed in SSCs 1&2.

We argue that the nitrogen excess observed in SSCs 1&2 results from the ejection of CNO-cycled material during giant eruptions (i.e., nitrogen is naturally enriched relative to oxygen; K. Davidson et al. 1982, 1986; D. J. Hillier et al. 2001; N. Przybilla et al. 2010; A. Maeder et al. 2014). Previous studies (F. X. Timmes et al. 1995; A. Maeder & G. Meynet 2001) have demonstrated that this process can be important in the low-metallicity environment where the efficiency of rotational mixing in massive stars is significantly enhanced, facilitating the transport of CNO-processed material from the stellar core to the outer envelope well before the end of the main-sequence phase (i.e., $\lesssim 3$ Myr).

An immediate question is how many giant eruptions like η Carinae ($N_{\rm GE}$) are needed to account for the observed nitrogen enrichment. Adopting an initial abundance ratio of $\log(\mathrm{N/O})_i \simeq -1.4$, corresponding to the low-metallicity "tight plateau" without primary nitrogen enrichment, and a final abundance ratio of $\log(\mathrm{N/O})_f \simeq -1.3$ (the lower limit of our measurements), we estimate that $N_{\rm GE} \sim 6-25$ (see Appendix C for derivation details) is sufficient to explain the observed nitrogen enrichment. A similar analysis has been done in NGC 5253 (H. A. Kobulnicky et al. 1997), where they find ~ 12 giant eruptions are needed to reproduce the localized nitrogen enrichment. The inferred $N_{\rm GE}$ should be regarded as an upper limit, as we do not account for other physical mechanisms (e.g., winds from very massive stars with zero-age main-sequence masses of $100-1000\,M_\odot$; J. S. Vink 2023) that may also contribute to the observed nitrogen enhancement.

4.4.2. Fe/O *Abundance Ratio*

In addition to nitrogen enrichment, SSCs 1&2 also exhibit a relatively high Fe/O abundance ratio ($\log \mathrm{Fe/O} \sim -1.5$) compared to typical H II regions at similar low metallicities (J. E. Méndez-Delgado et al. 2024, see right panel of Figure 9). Nevertheless, SSCs 1&2 might be relatively iron-poor compared to other SSCs (see Section 3.2). This potential iron depletion indicates that CNO-cycled material from giant eruptions promotes the formation of abundant metallic dust (dominated by FeSi and Fe) within the CSM (e.g., H. P. Gail et al. 2005).

The $\log \mathrm{Fe/O}$ value for SSCs 1&2, as well as for other SSCs, is comparable to those observed in two local extremely low-metallicity galaxies, J0811+4730 and J1631+4426 (Y. I. Izotov et al. 2018; T. Kojima et al. 2021; J. E. Méndez-Delgado et al. 2024), where $12+\log(\mathrm{O/H}) \lesssim 7.1$. This may indicate iron enrichment from very massive stars ($M_* > 300\ M_\odot$; T. Kojima et al. 2021) and/or pair-instability supernovae, as seen in high N/O systems such as GN-z11 (M. Nakane et al. 2024), occurring before the onset of CCSNe. Nevertheless, we caution that such comparisons are subject to the

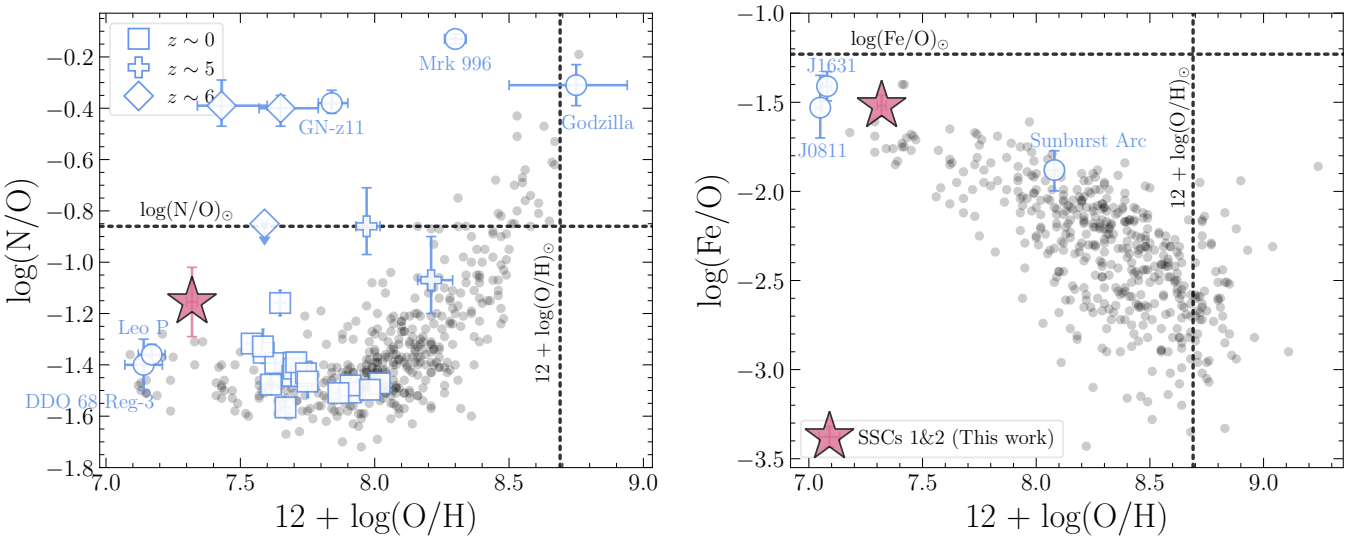


Figure 9. Nitrogen (*left*) and iron (*right*) abundances of J0337-0502 SSCs 1&2 (red star) are illustrated in the N/O-O/H and Fe/O-O/H panels, respectively. *Left:* We compare our nitrogen measurement to the local H II regions (gray circles) from L. S. Pilyugin et al. (2012), local metal-poor dwarf galaxies at $z < 0.04$ (blue squares) from D. A. Berg et al. (2019), high N/O galaxies at $z \sim 5$ (blue crosses; K. Z. Arellano-Córdova et al. 2024) and $z \sim 6$ (blue diamonds; H. Yanagisawa et al. 2024) observed by JWST, and several well-known high N/O galaxies at both low and high redshifts, including DDO 68 Region-3 (F. Annibali et al. 2019), Leo P (E. D. Skillman et al. 2013), GN-z11 (P. Senchyna et al. 2024), Mrk 996 (B. L. James et al. 2009), and Godzilla of the Sunburst Arc (M. Pascale & L. Dai 2024). *Right:* Our iron measurement is compared to the galaxy sample compiled by J. E. Méndez-Delgado et al. (2024) (gray circles), including two local extremely low-metallicity galaxies (J0811+4730 and J1631+4426; Y. I. Izotov et al. 2018; T. Kojima et al. 2021) and a known Lyman-continuum emitter in the Sunburst Arc ($z = 2.37$; B. Welch et al. 2025).

choice of Fe ICF adopted in the literature. For example, the J. E. Méndez-Delgado et al. (2024) sample uses the M. Rodríguez & R. H. Rubin (2005) Fe ICF, which can differ by ~ 0.2 dex from direct estimates based on all iron ionization states.

4.5. *Asymmetric Broad Wings in Balmer Lines*

The asymmetric broad wings of the Balmer line profiles in J0337-0502 were first discovered in the integrated Keck/ESI spectrum from Z. Peng et al. (2025). They find that the broad wings of Hβ exhibit a pronounced red excess–i.e., the red wing extends further in velocity space than the blue wing–and cannot be adequately fitted with either a Gaussian or a Lorentzian function. Our KCWI/KCRM observations confirm this result. Because the red wing of Hβ is blended with the blue wing of [O III] λ4959, we focus on the Hα broad wings with a higher SNR. Figure 10 shows that the Hα red wing extends to $\sim 10\,000$ km s^{-1}, whereas the blue wing reaches only $\sim -5\,000$ km s^{-1}. The observed $v_{\rm max}$ far exceeds the typical values ($v_{\rm max} \sim 1-2\times10^3$ km s^{-1}) predicted by both single-phase (T. A. Thompson et al. 2016) and multiphase (D. B. Fielding & G. L. Bryan 2022) galactic wind models.

Previous studies of η Carinae and of SNe IIn (e.g., K. Davidson et al. 1995; D. J. Hillier et al. 2001; A. Mehner et al. 2015; L. Dessart et al. 2009; R. M. Humphreys et al. 2012; C. Fransson et al. 2014; K. Davidson 2020) have demonstrated that the high-velocity, asymmetric broad wings arise from Thomson scattering. The observed red excess in the broad wings arises from the spherical divergence of the radially expanding flow (e.g., see Section 2.3 in C. Huang & R. A. Chevalier 2018).

To test this hypothesis, we employ the Monte Carlo Thomson-scattering framework of C. Huang & R. A. Chevalier (2018) (hereafter HC18)[11]. HC18 models adopt the Thomson scattering differential cross-section for each scattering event that occurs in a fully ionized medium with uniform temperature $T_{e,\rm CSM}$, in the shape of a spherical shell spanning radii R_1 to R_2. The medium has an Thomson-scattering optical depth τ_e measured in the radial direction. We adopt an r^{-2} density profile for the scattering medium, representing a constant pre-eruption mass outflow. We apply a constant outflow velocity by ignoring the radiative shock acceleration ($v_{\rm sh} \sim 0$), which is only significant shortly after the shock breakout.

We explore the parameter space in τ_e and shell-radius ratio $\eta = R_2/R_1$ from 1 to 10, and CSM expansion velocity v_w from 0 to 1 000 km s^{-1} to identify the combina-

[11] The publicly available code provided by HC18 can be accessed at https://github.com/Huang-CL/elsc/

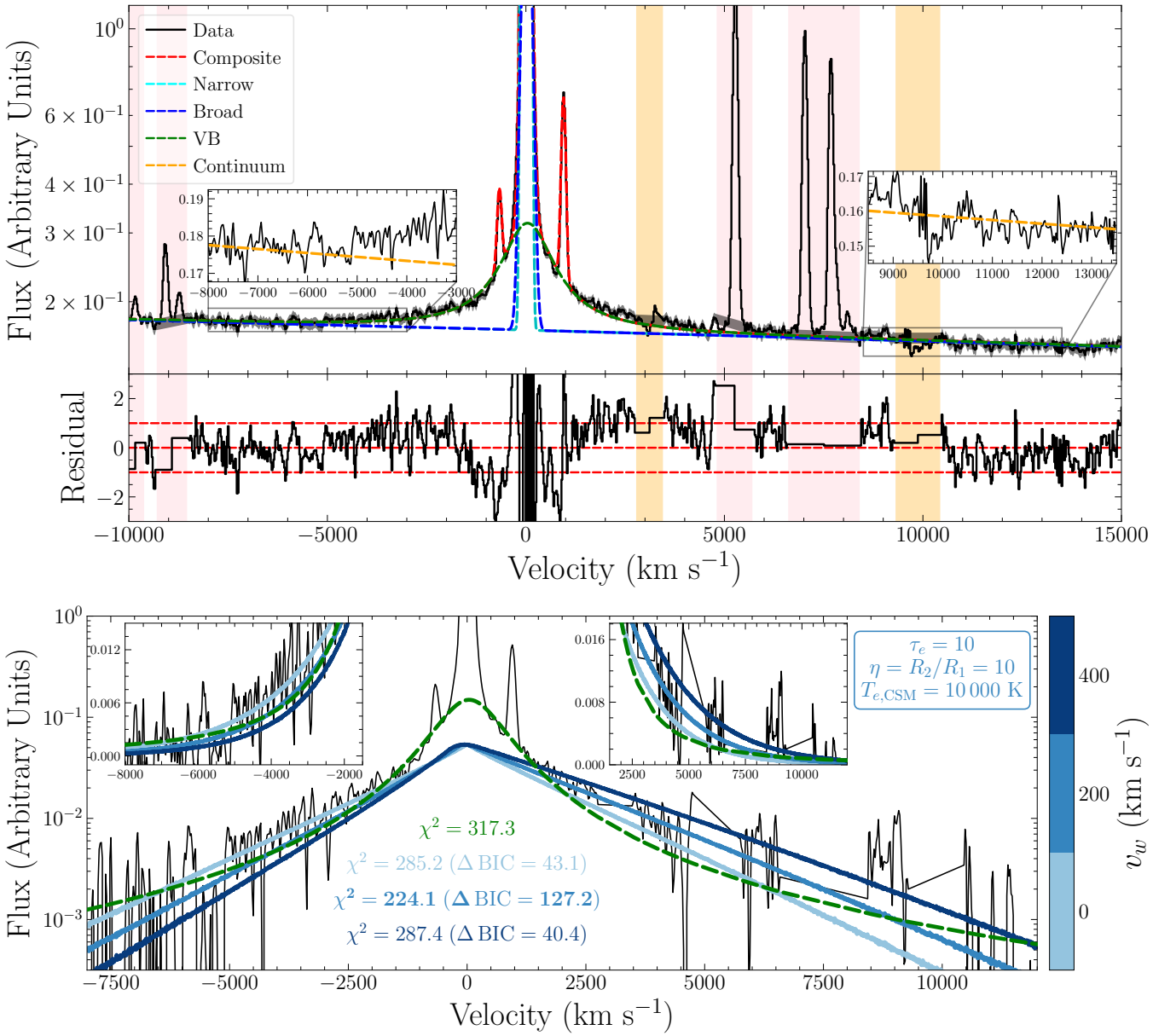


Figure 10. Asymmetric Hα broad wings with a red excess. *Top*: The best-fitting dGL model (red dashed line) is plotted alongside the observed line profile (black solid line). The narrow, broad, and VB emission velocity components are shown as cyan, blue, and green-dashed lines. Grey shading indicates the 1σ uncertainties of the raw data. Strong emission lines (or bad sky-subtraction features) next to the intended lines are masked during line fittings and are shaded in pink (or yellow). By visual inspection, the blue and red wings reach the best-fit continuum (orange dashed line) at $\sim -5\,000$ km s^{-1} and $\sim 10\,000$ km s^{-1}, respectively. Perturbing the line profile 1 000 times based on the error spectrum and adopting a 1σ detection threshold yields $v_{\mathrm{max}} = -5\,370^{+140}_{-70}$ km s^{-1} (blue) and $9\,940^{+50}_{-90}$ km s^{-1} (red), consistent with the visual estimate. The residual plot (data - model / error) is displayed in the second row. The 1σ residuals are indicated by red dashed lines. *Bottom:* Comparison between the best-fit Lorentzian profile (green dashed) for the VB component and the HC18 models color-coded at different v_w (see Section 4.5). The χ^2 values for the Lorentzian profile and the HC18 models, along with the corresponding difference in the Bayesian Information Criterion (ΔBIC = BIC$_{\mathrm{Lorentzian}}$ − BIC$_{\mathrm{HC18}}$; M. Newville et al. 2021), are displayed in the panel.

tion that best reproduces the observed Hα broad-wing profile. The bottom panel of Figure 10 shows the HC18 Thomson-scattering models at v_w from 0 to 400 km s^{-1}. These models are normalized to the peak flux in the broad-wing region, using the blue-wing velocity interval $\sim -5\,000$ to $\sim -1\,000$ km s^{-1} and the red-wing interval $\sim 1\,500$ to $\sim 10\,000$ km s^{-1}, thereby avoiding contamination by [N II] $\lambda\lambda$6548, 6583. We find that the HC18 model with $v_w = 200$ km s^{-1}, $\tau_e = 10$, and $\eta = 10$ yields the lowest χ^2 within the broad-wing region.

This conclusion is further supported by the comparison between the observed blue-to-red flux ratio ($F_{v<-1500}/F_{v>1500}$) in the broad wings (0.57 ± 0.10), defined as the integrated flux for $v < -1\,500$ km s^{-1} relative to $v > 1\,500$ km s^{-1}, and those of HC18 models at different v_w. Figure 11 shows that $F_{v<-1500}/F_{v>1500}$ decreases with increasing v_w, and that the setup $v_w = 200$ km s^{-1} best reproduces the observed ratio, being insensitive to the choice of τ_e in the case of large η considered in this study. This result is in agreement with our χ^2 analysis shown in Figure 10.

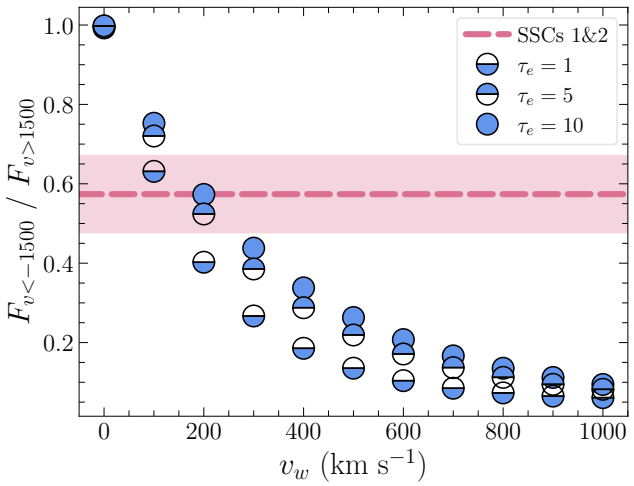


Figure 11. Observed blue-to-red flux ratio in the broad wings (red line) compared to those of HC18 models (blue points) at $\tau_e = 1$, 5, and 10 with $\eta = 10$ and $T_{e,\rm CSM} = 10\,000$ K.

One caveat of the HC18 Thomson scattering model is its assumption of spherical symmetry. In contrast, observations of systems such as η Carinae indicate the presence of a dense, bipolar-shaped CSM (e.g., K. Davidson & R. M. Humphreys 2012; K. Davidson 2020). However, the physical mechanism responsible for producing the red excess in emission-line profiles does not inherently require spherical symmetry, but rather a radially outward-expanding CSM like η Carinae. Therefore, our inferred τ_e from the best-fit HC18 model may only reflect the densest regions of the CSM if the CSM shares a similar non-spherically symmetric geometry to η Carinae, and τ_e could be significantly less than 10 in other directions (i.e., $\tau_{e,\rm max} \sim 10$).

Furthermore, we find that the [O III] λ5007 line extracted from the Keck/ESI observation of SSCs 1&2 (see Appendix D; Z. Peng et al. 2025) exhibits a relatively smaller $v_{\rm max}$ ($\sim 5\,000$ km s^{-1}) than Hα ($\sim 10\,000$ km s^{-1}). This discrepancy likely suggests that the broad wings of [O III] λ5007 do not arise from Thomson scattering within the dense CSM, since in that case one would expect a similar $v_{\rm max}$ to Hα. Moreover, the forbidden [O III] λ5007, with a critical density of $n_{\rm crit} \sim 10^6$ cm^{-3} (D. E. Osterbrock & G. J. Ferland 2006), would become strongly collisionally de-excited and approaches saturation within the dense CSM, whereas permitted lines such as Hα (i.e., with a much higher $n_{\rm crit}$ of $\sim 10^{15}$ cm^{-3}) continue to increase in emissivity with density in this regime (D. E. Osterbrock 1988).

Therefore, the broad wings of [O III] λ5007 likely originate from lower-density ejecta located outside the bipolar CSM, analogous to the outer ejecta of η Carinae beyond the Homunculus (with an average density $\gtrsim 500$ cm^{-3}), which reach velocities of $\sim 2\,000 - 6\,000$ km s^{-1} (K. Davidson et al. 1984; N. Smith & J. A. Morse 2004; N. Smith 2008). The driving mechanism of this fast outer ejecta remains uncertain. For example, N. Smith (2008) propose a core-explosion blast wave, possibly triggered by pulsational pair instability, while alternative scenarios suggest that such high velocities could arise from shocks accelerating outward through the steep density gradient in the star's outer layers and wind (K. Davidson 2012).

5. DISCUSSIONS

Based on the spectroscopically-derived properties (Section 3), we explore the potential giant eruption signatures and propose a coherent picture for the giant eruption in SSCs 1&2 in Section 4. To further discuss the proposed giant eruption picture, we present order-of-magnitude estimates of the CSM properties in Section 5.1. In Section 5.2, we also discuss whether the observed spectroscopic features of SSCs 1&2 can be reproduced by the existence of an AGN. Last but not least, due to the detection of O I λ8446, we illustrate the significance of Lyα radiation pressure in SSCs 1&2 in Section 5.3.

5.1. *Crude Estimations of CSM Properties*

In this section, using an analytical framework for CSM shock interaction (T. J. Moriya et al. 2013), we estimate a shock radius of $R_{\rm sh} \sim 10^{16}$ cm and a bolometric luminosity of the CSM interaction of $L_{\rm CSM} \sim 10^{41}$ erg s^{-1} at the observation epoch (Section 5.1.1). We argue that radiative cooling from $L_{\rm CSM}$ can naturally explain the luminosities of the observed VH-ionization [Fe V] λ4227 line and the *Chandra* observation of the luminous X-ray point source (Section 5.1.2). We also explore if the high-density CSM can efficiently trap He II λ304 photons to enhance He II λ4686 emission in Section 5.1.3.

5.1.1. *Estimations of $R_{\rm sh}$ and $L_{\rm CSM}$*

We assume the dense CSM can be described by a steady wind with a pre-eruption mass-loss rate of $\dot{M}_w$ and a constant wind velocity of v_w before the giant eruption. This assumption gives a density profile of the CSM as

$$\rho_{\rm CSM} = \frac{\dot{M}_w}{v_w\ 4\pi r^2} = D\ r^{-2} \simeq 7.5\times10^{16}\ D_*\ r^{-2}\ {\rm g\ cm^{-3}}, \quad (1)$$

where $D_* = \dot{M}_{w,0.3}/v_{w,200}$, $\dot{M}_{w,0.3} = \dot{M}_w/0.3\ {\rm M_\odot\ yr^{-1}}$, and $v_{w,200} = v_w/200\,{\rm km\,s^{-1}}$. The normalization for v_w is taken from the best-fit value in our Thomson-scattering model (Section 4.5), and $\dot{M}_w$ is based on the value of η Carinae (N. Smith 2013). The density structure of the giant eruption ejecta can be described as $\rho_{\rm ej} \propto r^{-k}$ where we adopt a fiducial value of $k = 7$ that is roughly consistent with some SNe IIn candidates (e.g., C. Fransson et al. 2014).

Following this model setup, the asymptotic solution of the CSM shell position, $R_{\rm sh}$, can be derived as:

$$R_{\rm sh} \simeq 2\times10^{16}\ \frac{M_{\rm ej,10}}{D_*} \left[-1+\left(1+0.9\sqrt{\frac{E_{\rm ej,51}}{M^3_{\rm ej,10}}}D_*t_1\right)^{1/2}\right]\ {\rm cm}. \quad (2)$$

Here, we normalize the giant eruption ejecta mass ($M_{\rm ej,10} = M_{\rm ej}/10\ M_\odot$), adopting the value based on the giant eruption of η Carinae (K. Davidson 2012), and the ejecta kinetic energy as $E_{\rm ej,51} = E_{\rm ej}/10^{51}$ erg. Assuming the shock interaction has persisted for $t \sim 5$ years ($t_1 \sim 5$), based on the observed duration of the NIR plateau (H26), we estimate a shock radius of $R_{\rm sh} \sim 1-1.5\times10^{16}$ cm for $E_{\rm ej,51} \sim 0.1-0.2$, comparable to that of η Carinae's giant eruption (K. Davidson 2012). This shock radius is consistent with the inner radius of our best-fit `CLOUDY` models (Section 4.2).

The bolometric luminosity of the CSM interaction at the observation epoch can be estimated as:

$$L_{\rm CSM} \simeq 7.5\times10^{42}\ \epsilon_{0.5}D_*\left(\frac{E_{\rm ej,51}}{M_{\rm ej,10}}\right)^{3/2} \left[1+0.9D_*\left(\frac{E_{\rm ej,51}}{M^3_{\rm ej,10}}\right)^{1/2}t_1\right]^{-3/2}\ {\rm erg\ s^{-1}}, \quad (3)$$

where $\epsilon_{0.5} = \epsilon/0.5$ is the conversion efficiency from kinetic energy to radiation for the CSM shock interaction (appropriate for the derived v_w and the CSM to giant eruption ejecta mass ratio like η Carinae; A. J. van Marle et al. 2010). Therefore, $L_{\rm CSM} \sim 0.6-1.3\times10^{41}\,{\rm erg\,s^{-1}}$ for $t_1 \sim 5$ and $E_{\rm ej,51} \sim 0.1-0.2$.

5.1.2. *Estimated Luminosities of [Fe V] and X-ray Point Source Emission*

Since both stellar and AGN models fail to reproduce the luminosity of the [Fe V] λ4227 line ($\simeq 3\times10^{37}$ erg s^{-1}), we propose that this emission may instead arise from the radiative cooling of the CSM interaction. By integrating the [Fe V] λ4227 emissivity—peaking at $\sim 10^5$ K—over 10^4-10^8 K and comparing it to the total radiative cooling rate across the same range, we estimate that $\sim 0.02-0.03\%$ of the cooling luminosity is emitted in [Fe V] λ4227 (S. Ploeckinger & J. Schaye 2020; G. Del Zanna et al. 2021). Therefore, we estimate the CSM interaction can produce an [Fe V] λ4227 luminosity of $\sim (1-4)\times10^{37}$ erg s^{-1} when $t_1 \sim 5$ and $E_{\rm ej,51} \sim 0.1-0.2$, in good agreement with the observed line luminosity. On the contrary, radiative cooling of this CSM interaction can only contribute to less than 50% of the observed [Fe IV] λ5234 line luminosity ($\sim 6\times10^{36}$ erg s^{-1}). Consequently, the majority of [Fe IV] λ5234 emission should originate from stellar photoionization (e.g., from the secondary hot star if the giant eruption candidate exists in a binary system), consistent with our `CLOUDY` modeling in Section 4.2.

Similarly, to compare with the *Chandra* observations (T. X. Thuan et al. 2004), we predict the X-ray luminosity in the $0.5-10$ keV band (corresponding to $T \sim 6\times10^6-10^8$ K), which is dominated by free-free bremsstrahlung cooling (C. Fransson et al. 2014; S. Ploeckinger & J. Schaye 2020), contributes to $\sim 3\%$ of the total cooling luminosity. This yields $L_{0.5-10\,{\rm keV}} \sim (2-4)\times10^{39}\,{\rm erg\,s^{-1}}$, in reasonable agreement with the *Chandra* measurement of $(2.8-3.5)\times10^{39}\,{\rm erg\,s^{-1}}$ (T. X. Thuan et al. 2004) for the X-ray point source. This estimation supports the interpretation that the X-ray point source originates from SSC 2 (T. X. Thuan et al. 2004; C. Kehrig et al. 2018), as the CSM interaction naturally reproduces its observed luminosity. The differing column densities inferred from the Thomson-scattering wings ($N_{\rm H,max} \sim 10^{25}\,{\rm cm^{-2}}$) and the *Chandra* X-ray data ($N_{\rm H} \sim 10^{22}\,{\rm cm^{-2}}$) could be explained by small-scale porosity in the CSM, which allows X-rays to leak through low-density channels (C. Fransson et al. 2014).

Furthermore, given our $\tau_{e,\,\rm max}$ constraint from Monte-Carlo simulations of asymmetric Hα line profile (Section 4.5), we can estimate an upper limit on the X-ray photon energy. Each Compton scattering reduces the photon energy (with an initial energy of E_0), and after approximately $N(\sim \tau^2_{e,\,\rm max})$ scatterings in the optically thick CSM, the remaining photon energy is roughly $E \approx m_ec^2/\tau^2_{e,\,\rm max} = 511/\tau^2_{e,\,\rm max}$ keV (when $E \ll E_0$; R. A. Chevalier & C. Fransson 2017). For $\tau_{e,\,\rm max} \sim 10$ (Figure 10), this corresponds to an upper energy limit of $E \approx 511/10^2$ keV ≈ 5 keV.

Hard X-ray emission can also arise from a dense ($n_e \gtrsim 10^{10}\,{\rm cm^{-3}}$) colliding-wind region in a massive binary system (located near $\sim 10^{13}$ cm relative to the primary

star), as proposed for η Carinae; however, its peak X-ray luminosity is only of order $L_{0.5-10\,\mathrm{keV}} \sim 10^{35}\,\mathrm{erg\,s^{-1}}$ (e.g., J. M. Pittard & M. F. Corcoran 2002; J. C. Martin et al. 2006; M. F. Corcoran & K. Ishibashi 2012). Therefore, although hard X-ray emission may originate from colliding-wind binaries, this mechanism might be far too faint to account for the observed luminosity of the X-ray point source.

5.1.3. *The Mystery of the Extreme He II Emission*

C. Kehrig et al. (2018) find that the extreme He II λ4686 emission of J0337-0502 can only marginally be explained by a `BPASS` (Binary Population and Spectral Synthesis) `v2.1` model (J. J. Eldridge et al. 2017) with a 0.05% $Z_\odot$ binary population ($\sim$ 1% of the derived gas-phase Z of SSCs 1&2) and a top-heavy initial mass function (IMF). Moreover, C. Kehrig et al. (2018) argue that the X-ray point source cannot provide a sufficient He II-ionizing photon rate, $Q(\mathrm{He^+})$, to account for the observed He II λ4686 emission in SSCs 1&2.

This conclusion should be reassessed in light of the high-density CSM found in this work. In such an extremely dense CSM, the He II λ4686 emission can be significantly enhanced by trapped He II λ304 ($\mathrm{He^+}$ 1s – 2p) photons in the $\mathrm{He^{++}}$ zone photoionized by soft X-ray photons from the CSM interaction (i.e., dominated by free-free bremsstrahlung). This trapping of He II λ304 photons substantially increase the population of $\mathrm{He^+}$ ions in the $n = 2$ level (i.e., similar to the effect of trapped Lyα in pumping the $n = 2$ level in neutral hydrogen; J. C. Martin et al. 2006).

We adapt the J. C. Martin et al. (2006) model (originally for the colliding-wind region of η Carinae) to our CSM parameters (see Appendix E for details). The He II λ4686 enhancement factor is quantified using the ratio of the line flux to the soft X-ray flux in the 54–550 eV band ($F(\mathrm{He\,II}\,\lambda4686)\,/\,\mathrm{F}(54-550\,\mathrm{eV})$), which increases with n_e (see their Figure 9). The intrinsic $L_{54-550\,\mathrm{eV}}$ can be extrapolated from the fixed-N_H ($\sim 10^{22}\,\mathrm{cm^{-2}}$) optically thin plasma model ($L_{54-550\,\mathrm{eV}} \sim 6 \times 10^{38}\,\mathrm{erg\,s^{-1}}$) for the hard X-ray point source in T. X. Thuan et al. (2004). To reproduce the observed He II λ4686 luminosity within SSCs 1&2 ($L_{4686} \simeq 3 \times 10^{38}$ erg s^{-1}, comparable to the value derived for the similar region "Knot B" in C. Kehrig et al. 2018), $F(\mathrm{He\,II}\,\lambda4686)/\mathrm{F}(54-550\,\mathrm{eV})$ must be ~ 0.5. This value exceeds the model prediction by factors of $\sim$ 10 given the estimated parameter values illustrated in Appendix E. Moreover, since the predicted $F(\mathrm{He\,II}\,\lambda4686)\,/\,\mathrm{F}(54\text{–}550\,\mathrm{eV})$ ratios should be regarded as upper limits (J. C. Martin et al. 2006), the extreme He II emission remains unexplained. Nevertheless, since many parameters in Appendix E are poorly constrained, future radiation-hydrodynamic simulations could self-consistently determine the He II λ4686 enhancement factor in the high-density CSM.

5.2. *AGN Possibilities*

We assess whether the emission-line properties of SSCs 1&2 can be explained by an AGN by examining three commonly invoked BLR/NLR mechanisms: self-Balmer absorption in dense clouds, collisional excitation affecting neutral helium lines, and optical forbidden iron emission from an AGN narrow-line region (NLR). As shown below, none of these scenarios simultaneously reproduces all observational constraints, and an AGN origin for the emission-line properties in SSCs 1&2 is therefore disfavored.

Self-Balmer Absorptions: Asymmetric Balmer-line profiles are typically observed in AGN. Various models are proposed to explain these asymmetric profiles, including deviation from a Keplerian motion, a binary super-massive BH, and an asymmetric distribution of the BLR clouds. In addition, C. M. Gaskell & P. Z. Harrington (2018) pointed out that partial obscuration of the BLR by compact dusty clumps can also produce these asymmetries. Similarly, for a dust-free cloud where a sufficiently high n_H can populate the $n = 2$ level of neutral hydrogen through collisional excitation, leading to significant self-Balmer absorption (e.g., H. Netzer & M. V. Penston 1976; G. Ferland & H. Netzer 1979; G. J. Ferland et al. 1979; A. Lawrence 1982; P. B. Hall 2007; I. Juodžbalis et al. 2024; K. Inayoshi & R. Maiolino 2025). The intensity of the Lyβ-fluorescence line O I λ8446 strongly depends on the population of the $n = 2$ level in H I and is commonly observed in the BLR (H. Netzer & M. V. Penston 1976). Nevertheless, this AGN interpretation implies a non-stellar Balmer break caused by significant absorption at wavelengths just blueward of the Balmer limit (rest wavelength at 3646 Å; K. Inayoshi & R. Maiolino 2025), which is not observed in our spectrum (Figure 2).

Collisional Excitations in He I lines: In addition, if we attribute the asymmetric Balmer-line profiles to the collisional excitation that populates the H I $n = 2$ state, we would also see enhancement in He I λ5876 and He I λ7065 due to collisional excitation from the $2\,^3S$ state of neutral helium. This picture is commonly proposed to explain the observed large He I/Hβ intensity ratio in the BLR (Y. Almog & H. Netzer 1989). However, we do not observe any broad component in our spectrum for He I λ7065, and He I λ5876 lies on the gap in the spectrograph.

To what extent will the collisional excitation affect the narrow components of neutral helium emission if they originate from the NLR? For a fiducial ionization parameter of $\log U = -2$ (see Appendix B for the AGN models run by `CLOUDY`) and $\log(\mathrm{He/H}) = 0.83\log(\mathrm{He/H})_\odot$ (i.e., $Y \simeq 0.25$), the `CLOUDY` model yields He I $\lambda5876/\mathrm{H}\beta = 0.13$ for density of $n_\mathrm{H} = 10^5$ cm^{-3} and increased slightly to

0.15 for $n_{\rm H} = 10^7$ cm^{-3}. Similarly, for the same density range, the He I λ7065/Hβ ratio increased from 0.10 to 0.12, consistent with that computed in G. Del Zanna & P. J. Storey (2022). As a reference, we measure He I λ7065/Hβ = 0.05 (0.04 for Y. I. Izotov et al. 2009) and Y. I. Izotov et al. (2009) measure He I λ5876/Hβ = 0.10. This implies that collisional excitation does not have a major effect on these neutral helium emission lines in SSCs 1&2, assuming a typical NLR density ($10^5 < n_{\rm H} < 10^7$ cm^{-3}).

Optical Forbidden Fe Lines: Optical [Fe II] emissions and high-ionization iron forbidden lines are commonly observed in Type I quasars (D. E. Osterbrock 1977), and are occasionally observed in Type II (obscured) quasars (M. Villar Martín et al. 2015). A. Rodríguez-Ardila et al. (2006) also reports the coronal lines that trace the gas outflow from a very highly ionized nuclear region of Seyfert galaxies. However, in Section 4.3, we demonstrate that our AGN models fail to reproduce the observed iron line ratios (e.g., [Fe III]/[Fe II] and [Fe IV]/[Fe III]) and significantly underestimate the luminosities of VH-ionization iron lines (e.g., [Fe V]).

In addition to the density and the ionization parameter (Figure 7), are these iron line ratios sensitive to the Fe abundance (if our iron abundance measurement suffers from significant systematic uncertainties)? To assess its impact, we explore a wide range of Fe abundance from 12+log(Fe/H) $\simeq$ 5.0 to 7.0. We find that our estimates for the iron line ratios are fairly robust regardless of the iron abundance we choose for the NLR cloud. Consequently, the inability of AGN models to reproduce the observed iron line ratios cannot be attributed to Fe abundance uncertainties.

5.3. *Lyα Radiation Pressure*

We argue that Lyα radiation pressure may be crucial for SSCs 1&2, where Lyα trapping is significant, as evidenced by the detection of the O I λ8446 line and the inferred $\tau_{\rm Ly\alpha} \sim 10^8$ from our `CLOUDY` model discussed in Section 4.2. In this scenario, the momentum injection rate from Lyα would dominate over the momentum budgets from Lyman Continuum (LyC) and UV photons prior to the onset of CCSNe and be approximately one dex higher than that from CCSNe in a low-metallicity ($Z \lesssim 0.05 Z_\odot$) environment during the first 10 Myr (T. Kimm et al. 2018).

We provide a crude comparison of momentum injection rates from Lyα radiation pressure and supernovadriven hot winds for a $\sim$ 3 Myr stellar population like SSCs 1&2. Following R. A. Chevalier & A. W. Clegg (1985), which describes a steady-state, adiabatic, spherically symmetric hot wind, we parameterize the total mass and energy injection rates as $\dot{M}_{\rm hot} = \eta_{\rm M}$ SFR and $\dot{E}_{\rm hot} \simeq 10^{40}$ erg s^{-1} $\eta_{\rm E}$ SFR/(M$_\odot$ yr^{-1}), respectively. $\eta_{\rm M}$ and $\eta_{\rm E}$ are the mass loading factor and the thermalization efficiency factor. The normalization of $\dot{E}_{\rm hot}$ assumes a simple stellar population (SSP) with a total stellar mass of $\sim 10^6$ $M_\odot$ and each CCSN deposits $E_{\rm SN} = 10^{51}$ erg (see Appendix B of Z. Peng et al. 2025). The momentum injection of hot wind, $\dot{p}_{\rm hot}$, can then be derived as

$$\dot{p}_{\rm hot} = \left(2\dot{E}_{\rm hot}\dot{M}_{\rm hot}\right)^{1/2} \simeq 0.5\ (\eta_{\rm E}\eta_{\rm M})^{1/2}\ \frac{L}{c}, \quad (4)$$

where $L \simeq 2000 L_\odot M_*/M_\odot$ is the bolometric luminosity for a $\lesssim$ 4 Myr SSP assuming a P. Kroupa (2001) IMF with a 300 $M_\odot$ high-mass cutoff (T. A. Thompson & T. M. Heckman 2024). If we assume $(\eta_{\rm E}\eta_{\rm M})^{1/2} \sim 0.5-1$, similar to M82, $\dot{p}_{\rm hot}/(L/c) \sim 0.25 - 0.5$.

Within a dustless and static medium, the Lyα momentum injection rate, $\tau_{\rm Ly\alpha}$, can be estimated based on Equation (34) in T. A. Thompson & T. M. Heckman (2024):

$$\begin{aligned}\dot{p}_{\rm Ly\alpha} &\simeq \tau_{\rm eff}\ \frac{L_{\rm Ly\alpha}}{c} \simeq \tau_{\rm eff}\ \frac{0.68\, L_{\rm ion}\, f_{\rm abs}}{c} \\ &\simeq 4\left(\frac{L}{c}\right)\ \frac{f_{\rm abs}\,\xi_{0.1}\,N_{\rm H,21}^{1/3}}{T_4^{1/3}}, \end{aligned} \quad (5)$$

where $\tau_{\rm eff} \simeq 100\, N_{\rm H,21}^{1/3}\, T_4^{-1/3}$ is the Lyα effective optical depth (equivalent to the Lyα force multiplication factor M_F; M. Dijkstra & A. Loeb 2008; T. Kimm et al. 2018; T. A. Thompson & T. M. Heckman 2024; O. Nebrin et al. 2025) and is valid for $\tau_{\rm Ly\alpha} \gtrsim 10^6$. Here $f_{\rm abs} = 1 - f_{\rm esc}$ denotes the Lyα absorption fraction, and $\xi_{0.1} = L_{\rm ion}/0.1L \simeq 3 - 5$ for the $\sim$ 3 Myr stellar population, where $L_{\rm ion}$ is the ionizing photon luminosity. Therefore, for $f_{\rm abs} \simeq 1$, $\log(N_{\rm H}/{\rm cm}^{-2}) \simeq 22$, and $T_4 \simeq 1$, $\dot{p}_{\rm Ly\alpha}/(L/c) \simeq 20 - 40$, which is a factor of $\sim 50 - 150$ larger than $\dot{p}_{\rm hot}$.

Based on our analysis in Section 4, we know that SSCs 1&2 have efficient dust formations and the dust-formation site (CSM) might radially expand at $\sim$ 200 km s^{-1}, suggesting the assumption of a dustless and static medium might break down. For a static, dust-filled medium where Lyα can be absorbed by dust grains, Equation (35) in T. A. Thompson & T. M. Heckman (2024) shows that $\dot{p}_{\rm Ly\alpha}$ would decrease to

$$\dot{p}_{\rm Ly\alpha} \simeq 1\left(\frac{L}{c}\right)\ \frac{f_{\rm abs}\,\xi_{0.1}}{f_{\rm dg,MW}^{1/4}\,T_4^{1/3}}, \quad (6)$$

where $f_{\rm dg,MW} = f_{\rm dg}/10^{-2}$ is the dust-to-gas mass ratio normalized to the Milky-Way value ($f_{\rm dg,MW} \simeq 0.1$ for J0337-0502; L. K. Hunt et al. 2014). For the fiducial parameter values adopted above, $\dot{p}_{\rm Ly\alpha}$ would decrease by a factor of four to $\dot{p}_{\rm Ly\alpha}/(L/c) \simeq 5 - 10$. Moreover, for a dustfree, radially expanding medium with $\log(N_{\rm H}/{\rm cm}^{-2}) \simeq 22$, extrapolating the relation among $\tau_{\rm eff}$, v_w, and $N_{\rm H}$ yields $\tau_{\rm eff} \sim 10$ (M. Dijkstra & A. Loeb 2008), or equivalently $\dot{p}_{\rm Ly\alpha}/(L/c) \simeq 1 - 2$. Considering both effects, $\dot{p}_{\rm Ly\alpha}$ would only be a factor of a few or even

comparable to $\dot{p}_{\rm hot}$ in a radially expanding, dust-filled medium.

Leveraging the cutting-edge analytical Lyα radiative transfer solution by O. Nebrin et al. (2025), which incorporates major Lyα suppression mechanisms (e.g., continuum absorption, gas velocity gradients), we find that M_F ranges from ~ 1 (uniform source) to ~ 60 (point source) given the observed nebular properties of SSCs 1&2 (e.g., $N_{\rm H}$ and $f_{\rm dg}$). This estimate is roughy consistent with the range of $\tau_{\rm eff}$ derived from the back-of-envelope calculations above.

In general, dust grains can be destroyed by intense UV radiation (S. C. Madden et al. 2006) and shocks (C. McKee 1989) after the onset of CCSNe. Conversely, grains can survive–or even grow–when they are embedded in $T \lesssim 10^4$ K ionized clouds entrained in the hot outflow (Z. Chen & S. P. Oh 2024). To fully assess the role of Lyα radiation pressure in a dusty, expanding medium, high-resolution multiphase simulations that self-consistently solve the dust dynamics are required (e.g., C.-Y. Hu et al. 2019).

The significant role of Lyα radiation pressure in SSCs 1&2 may offer valuable insights into the "luminosity-deficit" problem for the VB velocity component (FWHM $\sim 600 - 2500$ km s^{-1}), which originates from fast-outflowing galactic winds (Z. Peng et al. 2025). Z. Peng et al. (2025) demonstrate that while supernova-driven galactic wind models (T. A. Thompson et al. 2016; D. B. Fielding & G. L. Bryan 2022) can explain the $v_{\rm max}$ of the VB component observed in strong lines like Hα and [O III] λ5007, these wind models cannot account for the observed VB luminosities. Since we quantitatively show that Lyα resonant scattering can impart substantial momentum to the gas–potentially surpassing other feedback processes (e.g., CCSNe), particularly in extremely young, metal-poor systems–it is essential to incorporate Lyα radiation pressure when attempting to explain the VB luminosities in systems like SSCs 1&2.

6. SUMMARY AND CONCLUSION

Recent studies (e.g., H26) argue for the presence of an active massive BH in the blue compact dwarf galaxy SBS 0335-052 E based primarily on its observed NIR variability and broad Hα wings. Leveraging our recent KCWI/KCRM observation, we challenge this view by proposing that SSCs 1&2 of this galaxy show η Carinae-like giant eruption signatures instead. The main signatures of SSCs 1&2 can be summarized as follows:

1. The electron density constraint ($n_e \sim 10^6$ cm^{-3}) derived from the [Fe II] emission-line ratio reveal a dense paritally ionized region in SSCs 1&2. This dense gas resides in a CSM formed by pre-eruption stellar winds, which contains substantial warm dust ($\sim 400 - 500$ K) and accounts for the observed NIR excess.

2. The giant eruption candidate may reside in a binary system similar to η Carinae, where a secondary hot star ($T_{\rm eff} \sim 3.5-4.0\times10^4$ K) might provide the ionizing photons responsible for the [Fe IV] emission, while the primary, cool star ($T_{\rm eff} \sim 1.5 \times 10^4$ K) sustains the [Fe II] emission. The [Fe IV] emission also exhibits time variability. Higher-cadence observations will be necessary to confirm any periodic variability in [Fe IV] associated with the binary system and to distinguish it from enhanced emission driven by radiative cooling in the proposed CSM interaction during the giant-eruption phase (non-periodic).

3. Compared to other SSCs, the $\sim 0.1 - 0.2$ dex increase in $\log$ N/O for SSCs 1&2 suggests enrichment by CNO-cycled material ejected during multiple giant eruptions. The potential iron depletion in SSCs 1&2 (~ -0.3 to -0.1 dex in $\log$ Fe/O relative to other SSCs) is subject to systematic uncertainties in the adopted iron ICF; if confirmed, this depletion may indicate that CNO-cycled material facilitates the formation of abundant iron-rich dust.

4. We propose that the observed red-excess broad wings of Hα, extending from $\sim -5\,000$ km s^{-1} (blue) to $\sim 10\,000$ km s^{-1} (red) with a blue-to-red wing flux ratio of 0.57 ± 0.10, can be explained by Thomson scattering in the radially expanding ($v_w \sim 200$ km s^{-1}), optically thick ($\tau_e \sim 10$) CSM of size $\sim 10^{17}$ cm.

5. We find that radiative cooling from the proposed CSM shock interaction can naturally explain the luminosities of the observed VH-ionization [Fe V] λ4227 emission (and potentially contribute to the extreme He II λ4686 emission), as well as the *Chandra* observation of the luminous X-ray point source.

6. The detection of O I λ8446 and the inferred $\tau_{\rm Ly\alpha} \sim 10^8$ from our best-fit `CLOUDY` model suggest that the momentum injection rate of Lyα radiation can dominate over other momentum budgets (e.g., LyC, UV, and CCSNe), especially in a low-metallicity ($Z \lesssim 0.05 Z_\odot$) environment during the first 10 Myr.

Besides SSCs 1&2, the [Fe II] line ratio of SSC 3 also reveals a high-density PI region ($n_e \sim 10^6$ cm^{-3}), although these lines are detected at $< 3\sigma$. SSC 3 further exhibits a Wolf-Rayet blue bump (P. Papaderos et al. 2006; C. Kehrig et al. 2018) and hosts an older stellar population (~ 7 Myr), suggesting it appears to represent an analogous system to SSCs 1&2 but is observed at a more advanced evolutionary stage. In this scenario, the original donor star in the SSC 3 binary may have lost its hydrogen envelope through the binary interaction, becoming a WR star at the observation epoch. At the same time, the mass gainer evolves into an LBV and could ultimately explode as a Type IIn supernova (S. J. Kenyon & J. S. Gallagher 1985; N. Smith 2017b; K. Weis & D. J. Bomans 2020).

The recently approved JWST Cycle-4 proposal CLASSY+IR (CLASSYIR; PI: Danielle Berg) will obtain MIRI spectra covering 5 to 28 μm for 31 local star-forming galaxies. Future studies can investigate IR time variability from warm dust formation by comparing with archival IR photometry and identify high-density CSM via the [Fe II] emission-line ratio in extremely young ($\lesssim$ 3 Myr) SSCs of the CLASSY galaxies (D. A. Berg et al. 2022), thereby revealing systems analogous to SSCs 1&2 in J0337-0502.

ACKNOWLEDGMENTS

Z.P. appreciates the insightful discussions with Adam Carnall, Zirui Chen, Jared Goldberg, Daichi Hiramatsu, Kantapon Jensangjun, John Martin, and the ENIGMA group at UC Santa Barbara and Leiden University. Z.P. sincerely acknowledges support for this work from NASA FINESST (Future Investigators in NASA Earth and Space Science and Technology) grant 80NSSC23K1450. Z.Z. acknowledges financial support from NASA FINESST grant 80NSSC22K1755. T.W. acknowledges and thanks support by the National Science Foundation through grant PHY-2309135, and by the Gordon and Betty Moore Foundation through grant GBMF5076. The authors are grateful to the anonymous referee for providing constructive suggestions. The data presented herein were obtained at the W. M. Keck Observatory, which is operated as a scientific partnership among the California Institute of Technology, the University of California, and the National Aeronautics and Space Administration. The Observatory was made possible by the generous financial support of the W. M. Keck Foundation. The authors wish to recognize and acknowledge the very significant cultural role and reverence that the summit of Maunakea has always had within the indigenous Hawaiian community. We are most fortunate to have the opportunity to conduct observations from this mountain.

AUTHOR CONTRIBUTIONS

Z.P. and C.M. proposed the observing run. Z.P. reduced the data, formulated the initial research idea, performed the formal analysis and validation, and wrote the manuscript. C.M. helped significantly improve the writing and structure of the manuscript. J.H. and J.F.H. contributed to discussions regarding the possibility of an AGN in this target. N.P. developed the `KCWIKIT` package and Z.Z. developed the `KSkyWizard` package, both of which are essential for reducing the KCWI/KCRM data. C.H. helped fine-tune the Thomson-scattering model to simulate the asymmetric broad Hα wings. Y.L. drizzled the archival *HST* images and created the color-composite image. T.W. provided input on the validity of the stellar physics involved in this work. All authors discussed the results and provided comments on the manuscript.

Facilities: Keck:II (KCWI)

Software: `Astropy` (Astropy Collaboration et al. 2022), `CHIANTI` (G. Del Zanna et al. 2021), `LMFIT` (M. Newville et al. 2021), `Matplotlib` (J. D. Hunter 2007), `NumPy` (C. R. Harris et al. 2020), `pandas` (T. pandas development team 2020), `pyCloudy` (C. Morisset 2013), `PyNeb` (V. Luridiana et al. 2013, 2015), `PypeIt` (J. X. Prochaska et al. 2020), `SciPy` (P. Virtanen et al. 2020), `VerEmisFitting` (Z. Peng & Y. Li 2024)

APPENDIX

A. NEBULAR PROPERTIES OF SSCS

Table 3 shows SSCs' nebular properties derived from our extracted KCWI/KCRM spectra using the adopted methodologies described below. The best-fit n_e, T_e, and $\log U$ values of low, intermediate, and high ionization zones for SSCs 3 to 8 are summarized in Figure 12 (those of SSCs 1&2 are summarized in Figure 3).

A.1. *Extinction*

To correct for Galactic foreground extinction, we obtain $E(B-V)_{\rm MW} = 0.0402 \pm 0.002$ from the dust maps of E. F. Schlafly & D. P. Finkbeiner (2011) and apply the correction using the Galactic extinction curve interpolated from Table 3 of E. L. Fitzpatrick (1999). We then model the intrinsic dust attenuation using the SMC extinction law (K. D. Gordon et al. 2003). The SNR-weighted intrinsic color excess, $E(B-V)_{\rm int}$, is derived by comparing the observed recombination line ratios—specifically, Hδ/Hγ, H9/Hγ, H10/Hγ, and Paschen lines Pa 9 through Pa 18 relative to Hγ to the theoretical Case B ratios from P. J. Storey & D. G. Hummer (1995). These chosen relatively high-order Balmer and Paschen lines are free from contamination by nearby strong lines or obvious Thomson-scattering broad wings that are seen in Hα and Hβ (Section 4.5). The measured $E(B-V)_{\rm int}$ value for SSCs 1&2 is 0.06 ± 0.01, whereas the remaining SSCs are consistent with zero internal reddening (i.e., $E(B-V)_{\rm int} = 0$).

A.2. *Ionization-Zone Definitions and Diagnostics*

We use the GETCROSSTEMDEN method in `PyNeb` (V. Luridiana et al. 2013, 2015) to derive n_e and T_e for each ionization zone defined by B21. The ions used to con-

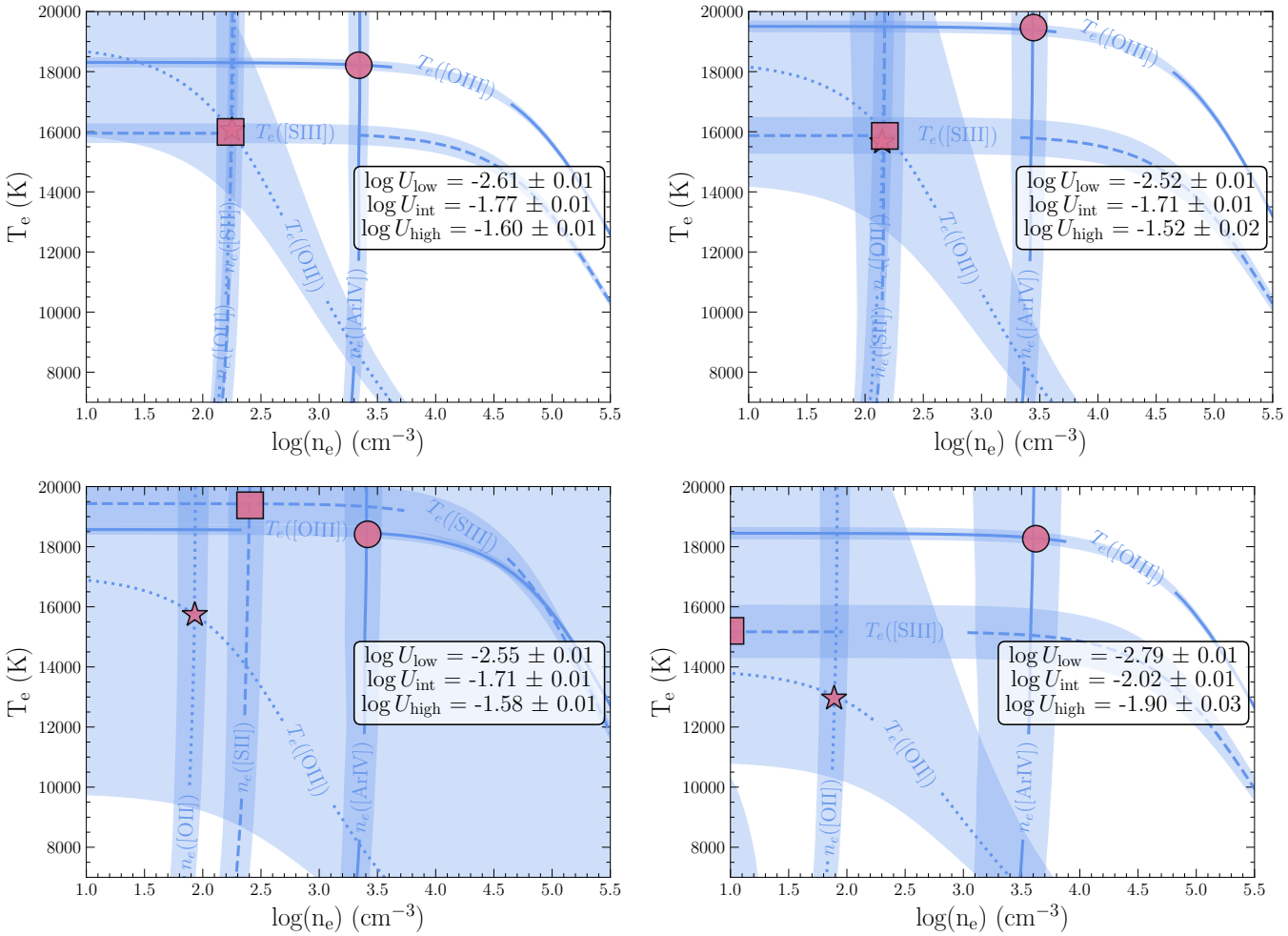


Figure 12. T_e and n_e solutions for SSC 3 (*top left*), SSCs 4&5&7 (*top right*), SSC 6 (*bottom left*), and SSC 8 (*bottom right*). The plotting style is identical to that of Figure 3. For SSC 8, the n_e in the intermediate-ionization zone, traced by the [S II] $\lambda\lambda$6716, 6731 doublet, approaches its low-density limit (10 cm^{-3}).

strain n_e and T_e in each ionization zone are summarized below:

- Low (14.5 – 20.6 eV): n_e ([O II]); T_e ([O II])
- Intermediate (23.3 – 34.8 eV): n_e ([S II]); T_e ([S III])
- High (35.1 – 54.9 eV): n_e ([Ar IV]); T_e ([O III])
- Very-High (VH; > 54.4 eV): n_e ([Ar IV]); T_e ([Fe V])$_{CL}$

Notably, we use the ratio of the [S II] $\lambda\lambda$6716, 6731 doublet to estimate the electron density of the intermediate ionization zone, as the [Cl III] $\lambda\lambda$5517, 5537 doublet (B21) falls outside the wavelength coverage of our KCWI/KCRM spectra (i.e., it lies too close to the dichroic).

Moreover, since the temperature-sensitive [Ne III] λ3342 line of the VH ionization zone lies outside our wavelength coverage, we adopt the ion-fraction-weighted temperature of [Fe V] from the best-fitting `CLOUDY` models (M. Chatzikos et al. 2023, Section 4) to determine T_e ([Fe V])$_{CL}$ (e.g., $\sim$ 23 000 for SSCs 1&2).

Besides these zones with ionization potential energies $\gtrsim$ 15 eV, we include an additional partially ionized (PI) zone—traced by [Fe II] emission ($\sim$ 8 – 15 eV; see Figure 2)—which originates in the densest, most shielded neutral regions near ionization and shock fronts (M. A. Bautista et al. 1994).

A.3. *Line-Ratio Constraints on* log U

We estimate the ionization parameter, log U, of low-to-intermediate (log U_{low}), intermediate-to-high (log U_{int}), and high-to-very-high ionization zones (log U_{high}) using the [S III]/[S II], [O III]/[O II], and [Ar IV]/[Ar III] ratios, respectively. These estimates are based on the polynomial relations between these line ratios and theoretical predictions of log U from `CLOUDY` models at different gas-phase metallicities, as presented in D. A. Berg et al. (2019) and B21.

The ionization-averaged log U, log U_{ave}, can characterize the degree of ionization in the nebulae within each SSC. log U_{ave} is obtained by weighting log U_{low} and

$\log U_{\rm high}$ by their respective oxygen ionization fractions measured in Appendix A.4. We derive $\log U_{\rm ave}$ value ranges from ~ -1.60 (SSCs 4&5&7) to ~ -2.10 (SSC 8).

A.4. *Ionic Abundances from Multiple Ionization Stages*

We apply the GETIONABUNDANCE method in `PyNeb` to derive ionic abundances from the detected emission lines and apply ICFs to account for ionization stages that are not directly observed.

For oxygen, we assume that $\mathrm{O/H} = \left(\mathrm{O}^{+} + \mathrm{O}^{+2}\right)/\mathrm{H}^{+}$ and derive O^{+} and O^{+2} ionic abundances using the [O II] $\lambda\lambda$3726, 29 doublet and [O III] λ4959 emission line, because contributions from O^{0} and O^{+3} are negligible in galaxies with physical properties (e.g., $\log U_{\rm ave}$ and gas-phase metallicity) similar to J0337-0502 (e.g., J1044+0353; B21).

For nitrogen, we derive the N^{+} ionic abundance from [N II] λ6583 and apply ICF(N^{+}) to account for higher ionization stages as the high-ionization UV N III] and N IV] lines at $\sim$ 1485 Å and $\sim$ 1750 Å, respectively, lie outside the wavelength coverage of our KCWI spectrum. We use the following three approaches to estimate ICF(N^{+}): (1) the relation between ICF(N^{+}), $\log U$, and Z derived in B21 (ICF(N^{+}) $\simeq$ 30 for $\log U_{\rm ave} = -1.67$ and $Z \simeq 0.05\,Z_{\odot}$), (2) the simple assumption that N^{+} and O^{+} share the same ionic fraction (ICF(N^{+}) = $\mathrm{O/O}^{+}$; M. Peimbert & R. Costero 1969), and (3) the empirical fit based on Milky Way H II regions (ICF(N^{+}) = $0.39 + 1.19 \times (\mathrm{O/O}^{+})$; C. Esteban et al. 2020).

For iron, we determine the Fe^{+} ionic abundance using both [Fe II] λ5262 and [Fe II] λ8617, for which Lyα or UV-continuum pumping effects are negligible. Systematic uncertainties arising from the choice of [Fe II] lines are included in the errors listed in Table 3. We then use [Fe III] λ4658 and [Fe IV] λ5234, which are deblended from other strong emission lines such as Hβ and the [O III] doublet, to derive the ionic abundances of Fe^{+2} and Fe^{+3}, respectively. Finally, to constrain the Fe^{+4} ionic abundance, we use [Fe V] λ4227, which has been detected in other extreme emission-line galaxies like J1044+0353 and J1418+2102 (B21). For the other SSCs without detections for all ionization stages from Fe^{+} to Fe^{+4}, we use ICF(Fe^{+2}+Fe^{+4}) for SSCs 3 to 7 and ICF(Fe^{+2}) for SSC 8, which are both functions of metallicity and $\log U$ (Figure 7 in B21).

B. AGN MODELS

We run a set of `CLOUDY` models with the ionizing photons follow the SED with the "strong UV bump" in T. Nagao et al. (2006). We adopt a wide range for the gas density, $n_{\rm H} = 10^{5} - 10^{7}$ cm^{-3}, assuming that the narrow (FWHM $\lesssim$ 100 km s^{-1}) emission lines originate from the Narrow-line region (NLR) of an AGN. For the NLR cloud, we use a plane-parallel model with constant density with column density of $N_{\rm H} = 10^{23}$ cm^{-2} (H26). We vary the ionization parameter from $\log U = -6.0$ to -0.5. For consistency with previous analysis, we assume $Z = 0.04\ Z_{\odot}$ (Section 3.2) and the α-abundance metallicity scales with the solar abundance. We also set the heavy element mass ratio and micro-turbulence velocity to zero for simplicity.

C. CRUDE ESTIMATIONS OF $N_{\rm GE}$

We estimate $N_{\rm GE}$ required to produce the observed nitrogen enrichment in SSCs 1&2 using a simple order-of-magnitude argument, explicitly stating the assumptions below.

1. Oxygen abundances remain relatively constant before the onset of CCSNe, as the newly-formed oxygen produced by CNO-cycled material from giant eruptions is negligible compared to the initial gas-phase oxygen mass (e.g., the nitrogen-to-oxygen stellar yield ratio $y_{\rm N}/y_{\rm O} \sim 50$ for a 60 $M_{\odot}$ star in CNO-cycle equilibrium; H. J. G. L. M. Lamers et al. 2001).

2. The CNO-cycled ejecta mix uniformly with the surrounding ISM within $\sim$ 3 Myr, which is justified by the characteristic giant eruption ejecta temperatures of 10 000 K and rapid mixing (H. A. Kobulnicky et al. 1997).

Under these assumptions, the change in nitrogen-to-oxygen number density is approximately equal to the change in nitrogen mass density relative to hydrogen ($Z_{\rm g,N}$):

$$\Delta \log (\mathrm{N/O}) = \log (\mathrm{N/O})_{f} - \log (\mathrm{N/O})_{i} = \log R_{\rm N/O} \sim \Delta \log Z_{\rm g,N} = \log\left(1 + \frac{y_{\rm N}\ M_{\rm ej,tot}}{M_{\rm g,N}}\right) = \log\left(1 + \frac{y_{\rm N}\ N_{\rm GE}\ M_{\rm ej}}{Z_{g,\rm N}\ M_{g}}\right). \tag{C1}$$

Here, M_g is the total gas mass, $y_{\rm N} \sim 10^{-3}$ from the CNO cycle (D. R. H. Johnson et al. 1992; G. Meynet & A. Maeder 2002; N. Prantzos et al. 2018), and $M_{\rm ej,tot} = N_{\rm GE}\,M_{\rm ej}$ is the cumulative ejecta mass from multiple giant eruptions.

Assuming $\log(\mathrm{N/O})_{i} \simeq -1.4$ and $\log(\mathrm{N/O})_{f} \simeq -1.3$ (Section 4.4), we obtain $R_{\rm N/O} \simeq 1.25$. Solving Equation C1 then yields

$$N_{\rm GE} \sim \frac{(R_{\rm N/O} - 1)\, Z_{\rm g,N}\, M_{g}}{y_{\rm N}\, M_{\rm ej}} \sim 6 - 25, \tag{C2}$$

where we adopt $M_{\rm ej} \sim 10 - 40\,M_{\odot}$ (K. Davidson 2012) and $Z_{\rm g,N} M_{g} \sim 1$ for a gas fraction $\mu \simeq 0.95$ (R. I. Thompson et al. 2009) and $M_{*} \sim 10^{6}\,M_{\odot}$ (Table 2). We caution, however, $N_{\rm GE}$ may easily vary by a factor of a few, given that $R_{\rm N/O}$, $y_{\rm N}$, and $M_{\rm ej}$ are not well constrained by observations or simulations.

D. BROAD WINGS IN Hα AND [O III] λ5007 FROM THE ESI SPECTRUM OF SSCS 1&2

Figure 13 presents the best-fit dGL models for the [O III] λ5007 (top) and Hα (bottom) line profiles from

the Keck/ESI spectrum (Z. Peng et al. 2025) of SSCs 1&2.

E. OVERVIEW OF THE ENHANCED He II λ4686 MODEL

In the framework of J. C. Martin et al. (2006), the He II λ4686 emission in the He^{++} zone can be strongly amplified by three coupled radiative pumping mechanisms once the He II λ304 transition becomes optically thick. First, resonant trapping of λ304 photons overpopulates the He^{+} $n = 2$ level, enabling efficient photoionization from $n = 2$ by UV photons. Second, at large optical depth in the He II λ1215 emission, almost every decay from $n = 4$ goes through $n = 3$, increasing He II λ4686 emission. Third, trapped Lyα photons can excite He^{+} from $n = 2$ to $n = 4$ at $v_{\rm He\,II} \approx -120\,{\rm km\,s^{-1}}$ (this contribution is negligible at $n_e \lesssim 10^{9.5}\,{\rm cm^{-3}}$). We refer readers to Section 8 and Appendix B in J. C. Martin et al. (2006) for details.

The key parameters that influence the enhancement factor (i.e., $F({\rm He\,II}\,\lambda4686)\,/\,{\rm F}(54-550\,{\rm eV})$) include:

1. Assuming homologous expansion (i.e., $v \propto r$), the expansion parameter $\eta \sim v_w/R_2 \sim 10^{-10}\,{\rm s^{-1}}$ determines the optical depth of He II λ304 emission under the Sobolev approximation (i.e., $\tau_{\lambda304} \propto 1/\eta$).

2. The corresponding incident energy flux of photons between 54 and 550 eV, $F_{54-550\,{\rm eV}} \sim L_{54-550\,{\rm eV}}/(4\pi f_\Omega r^2) \sim 10^{20}\,{\rm eV\,cm^{-2}\,s^{-1}}$, for the optically thin plasma model. Here we assume a fiducial r of $0.1\,R_{\rm sh} \sim 10^{15}$ cm, corresponding to the approximate width between the CDS and the forward shock (R. A. Chevalier & C. Fransson 1994). We define $f_\Omega \equiv \Omega/4\pi$ as the solid-angle covering fraction of the densest component of the CSM ($f_\Omega \sim 0.2$ for η Carinae; K. Davidson et al. 2001; N. Smith 2006).

3. The UV photoionization rate from the $n = 2$ level of He^{+} ions, A_{2c}, which is positively correlated with the enhancement factor when $n_e \lesssim 10^{10}\,{\rm cm^{-3}}$. In J. C. Martin et al. (2006), $A_{2c} \approx 10^4\,{\rm s^{-1}}$ is determined solely by stellar UV photons from the binary system; however, in the CSM scenario considered here, the stellar contribution to A_{2c} is reduced by a factor of $\sim 10^5$ as the characteristic radius increases from ~ 2.5 AU (for the colliding-wind case) to $R_{\rm sh} \sim 10^{16}$ cm. We estimate A_{2c} arising from X-ray photoionization associated with the CSM interaction by running `CLOUDY` models with a bremsstrahlung (optically thin plasma) incident spectrum, based on the fixed-$N_{\rm H}$ model of T. X. Thuan et al. (2004). We assume $r_{\rm in} = 10^{15}$ cm, a r^{-2} density profile (Equation 1) with an initial density of $10^9\,{\rm cm^{-3}}$ (corresponding to $\tau_{e,\,\rm max} \sim 10$), a total luminosity of $10^{41}\,{\rm erg\,s^{-1}}$ (Section 5.1.1), and a CNO-cycled abundance pattern. We find that $A_{2c} \sim 10$ within the He^{++} zone.

REFERENCES

Adamo, A., Zackrisson, E., Östlin, G., & Hayes, M. 2010, ApJ, 725, 1620, doi: 10.1088/0004-637X/725/2/1620

Almog, Y., & Netzer, H. 1989, MNRAS, 238, 57, doi: 10.1093/mnras/238.1.57

Annibali, F., La Torre, V., Tosi, M., et al. 2019, MNRAS, 482, 3892, doi: 10.1093/mnras/sty2911

Arellano-Córdova, K. Z., Cullen, F., Carnall, A. C., et al. 2024, arXiv e-prints, arXiv:2412.10557, doi: 10.48550/arXiv.2412.10557

Asplund, M., Amarsi, A. M., & Grevesse, N. 2021, A&A, 653, A141, doi: 10.1051/0004-6361/202140445

Astropy Collaboration, Price-Whelan, A. M., Lim, P. L., et al. 2022, ApJ, 935, 167, doi: 10.3847/1538-4357/ac7c74

Bautista, M. A., Pradhan, A. K., & Osterbrock, D. E. 1994, ApJL, 432, L135, doi: 10.1086/187530

Berg, D. A., Chisholm, J., Erb, D. K., et al. 2021, The Astrophysical Journal, 922, 170, doi: 10.3847/1538-4357/ac141b

Berg, D. A., Erb, D. K., Henry, R. B. C., Skillman, E. D., & McQuinn, K. B. W. 2019, ApJ, 874, 93, doi: 10.3847/1538-4357/ab020a

Berg, D. A., James, B. L., King, T., et al. 2022, The Astrophysical Journal Supplement Series, 261, 31, doi: 10.3847/1538-4365/ac6c03

Blum, R. D., Burleigh, K., Dey, A., et al. 2016, in American Astronomical Society Meeting Abstracts, Vol. 228, American Astronomical Society Meeting Abstracts #228, 317.01

Calzetti, D. 2013, in Secular Evolution of Galaxies, ed. J. Falcón-Barroso & J. H. Knapen, 419, doi: 10.48550/arXiv.1208.2997

Chatzikos, M., Bianchi, S., Camilloni, F., et al. 2023, RMxAA, 59, 327, doi: 10.22201/ia.01851101p.2023.59.02.12

Chen, Y., Steidel, C. C., Erb, D. K., et al. 2021, MNRAS, 508, 19, doi: 10.1093/mnras/stab2383

Chen, Z., & Oh, S. P. 2024, MNRAS, 530, 4032, doi: 10.1093/mnras/stae1113

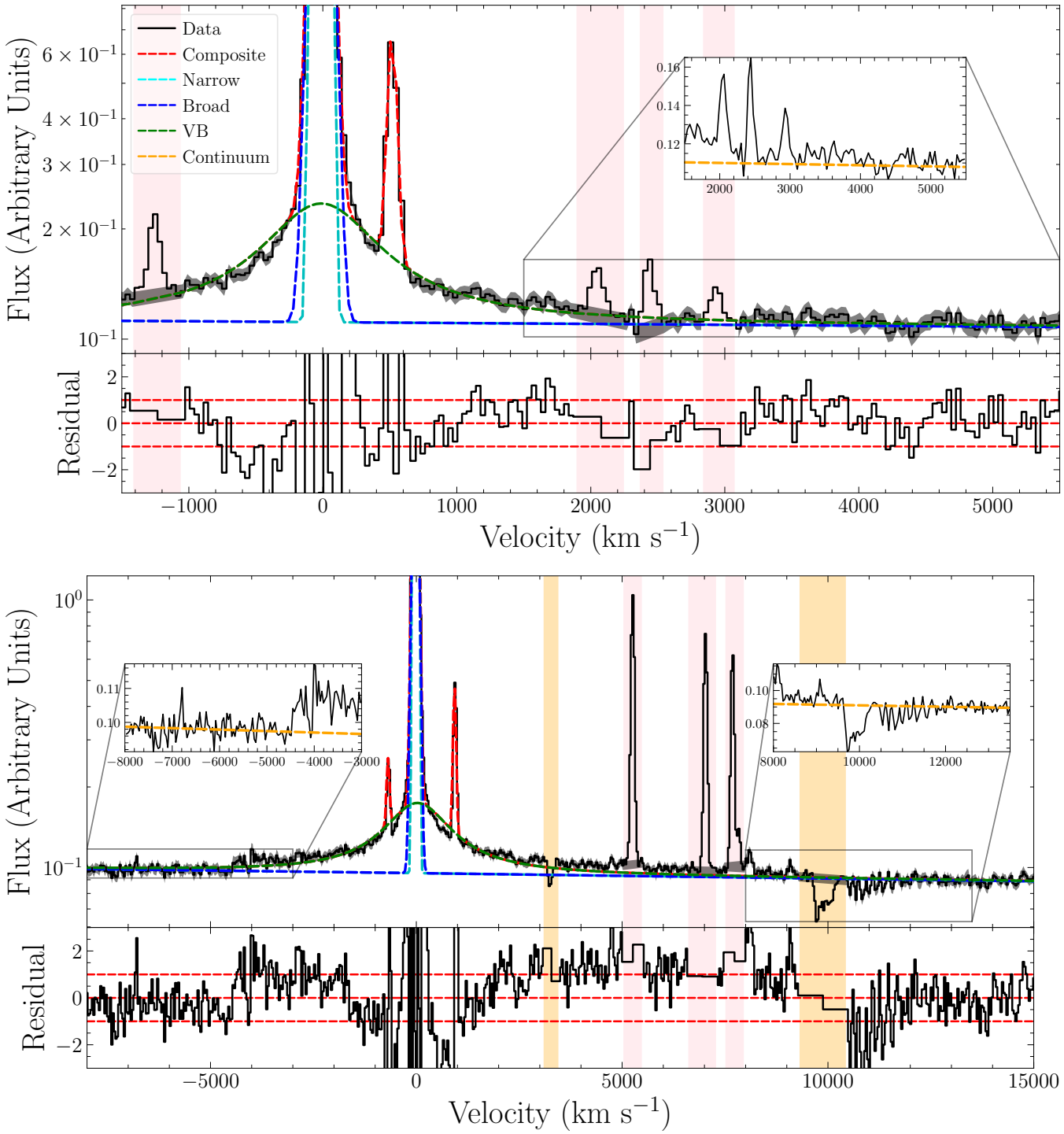


Figure 13. Broad Wings in [O III] λ5007 (*top*) and Hα (*bottom*) from the ESI Spectrum of SSCs 1&2. The plotting styles are consistent with those in Figure 10. If we perturb the [O III] λ5007 line profile 1 000 times based on the error spectrum and adopting a 1σ detection threshold yields $4\,850^{+140}_{-180}$ km s^{-1} for the red wing (the blue wing is blended with [O III] λ4959). The Hα profile exhibits a similar $v_{\rm max}$ as that observed in our KCWI/KCRM data (see Figure 10).

Chevalier, R. A., & Clegg, A. W. 1985, Nature, 317, 44, doi: 10.1038/317044a0

Chevalier, R. A., & Fransson, C. 1994, ApJ, 420, 268, doi: 10.1086/173557

Chevalier, R. A., & Fransson, C. 2017, in Handbook of Supernovae, ed. A. W. Alsabti & P. Murdin (Springer International Publishing), 875, doi: 10.1007/978-3-319-21846-5_34

Chisholm, J., Berg, D. A., Endsley, R., et al. 2024, MNRAS, 534, 2633, doi: 10.1093/mnras/stae2199

Choe, S., Emil Rivera-Thorsen, T., Dahle, H., et al. 2025, A&A, 698, A16, doi: 10.1051/0004-6361/202450685

Chugai, N. N. 2001, MNRAS, 326, 1448, doi: 10.1111/j.1365-2966.2001.04717.x

Corcoran, M. F., & Ishibashi, K. 2012, in Astrophysics and Space Science Library, Vol. 384, Eta Carinae and the Supernova Impostors, ed. K. Davidson & R. M. Humphreys, 195, doi: 10.1007/978-1-4614-2275-4_9

Davidson, K. 2012, in Astrophysics and Space Science Library, Vol. 384, Eta Carinae and the Supernova Impostors, ed. K. Davidson & R. M. Humphreys, 43, doi: 10.1007/978-1-4614-2275-4_3

Davidson, K. 2020, Galaxies, 8, 10, doi: 10.3390/galaxies8010010

Davidson, K., Dufour, R. J., Walborn, N. R., & Gull, T. R. 1984, in IAU Symposium, Vol. 105, Observational Tests of the Stellar Evolution Theory, ed. A. Maeder & A. Renzini, 261

Davidson, K., Dufour, R. J., Walborn, N. R., & Gull, T. R. 1986, ApJ, 305, 867, doi: 10.1086/164301

Davidson, K., Ebbets, D., Weigelt, G., et al. 1995, AJ, 109, 1784, doi: 10.1086/117408

Davidson, K., & Humphreys, R. M., eds. 2012, Astrophysics and Space Science Library, Vol. 384, Eta Carinae and the Supernova Impostors, doi: 10.1007/978-1-4614-2275-4

Davidson, K., & Smith, N. 2000, Nature, 405, 532, doi: 10.1038/35014740

Davidson, K., Smith, N., Gull, T. R., Ishibashi, K., & Hillier, D. J. 2001, AJ, 121, 1569, doi: 10.1086/319419

Davidson, K., Walborn, N. R., & Gull, T. R. 1982, ApJL, 254, L47, doi: 10.1086/183754

Del Zanna, G., Dere, K. P., Young, P. R., & Landi, E. 2021, ApJ, 909, 38, doi: 10.3847/1538-4357/abd8ce

Del Zanna, G., & Storey, P. J. 2022, MNRAS, 513, 1198, doi: 10.1093/mnras/stac800

Dessart, L., Hillier, D. J., Gezari, S., Basa, S., & Matheson, T. 2009, MNRAS, 394, 21, doi: 10.1111/j.1365-2966.2008.14042.x

Dey, A., Schlegel, D. J., Lang, D., et al. 2019, AJ, 157, 168, doi: 10.3847/1538-3881/ab089d

Dijkstra, M., & Loeb, A. 2008, MNRAS, 391, 457, doi: 10.1111/j.1365-2966.2008.13920.x

Duncan, R. A., White, S. M., Lim, J., et al. 1995, ApJL, 441, L73, doi: 10.1086/187793

Eldridge, J. J., Stanway, E. R., Xiao, L., et al. 2017, PASA, 34, e058, doi: 10.1017/pasa.2017.51

Esteban, C., Bresolin, F., García-Rojas, J., & Toribio San Cipriano, L. 2020, MNRAS, 491, 2137, doi: 10.1093/mnras/stz3134

Ferland, G., & Netzer, H. 1979, ApJ, 229, 274, doi: 10.1086/156952

Ferland, G. J., Netzer, H., & Shields, G. A. 1979, ApJ, 232, 382, doi: 10.1086/157297

Fielding, D. B., & Bryan, G. L. 2022, ApJ, 924, 82, doi: 10.3847/1538-4357/ac2f41

Fitzpatrick, E. L. 1999, Publications of the Astronomical Society of the Pacific, 111, 63, doi: 10.1086/316293

Fransson, C., Chevalier, R. A., Filippenko, A. V., et al. 2002, ApJ, 572, 350, doi: 10.1086/340295

Fransson, C., Ergon, M., Challis, P. J., et al. 2014, ApJ, 797, 118, doi: 10.1088/0004-637X/797/2/118

Gail, H. P., Duschl, W. J., Ferrarotti, A. S., & Weis, K. 2005, in Astronomical Society of the Pacific Conference Series, Vol. 332, The Fate of the Most Massive Stars, ed. R. Humphreys & K. Stanek, 323

Gaskell, C. M., & Harrington, P. Z. 2018, MNRAS, 478, 1660, doi: 10.1093/mnras/sty848

Gordon, K. D., Clayton, G. C., Misselt, K. A., Landolt, A. U., & Wolff, M. J. 2003, The Astrophysical Journal, 594, 279, doi: 10.1086/376774

Gull, T. R., Hillier, D. J., Hartman, H., et al. 2022, ApJ, 933, 175, doi: 10.3847/1538-4357/ac74c2

Hall, P. B. 2007, AJ, 133, 1271, doi: 10.1086/511272

Hamann, F. 2012, in Astrophysics and Space Science Library, Vol. 384, Eta Carinae and the Supernova Impostors, ed. K. Davidson & R. M. Humphreys, 95, doi: 10.1007/978-1-4614-2275-4_5

Harikane, Y., Zhang, Y., Nakajima, K., et al. 2023, ApJ, 959, 39, doi: 10.3847/1538-4357/ad029e

Harris, C. R., Millman, K. J., van der Walt, S. J., et al. 2020, Nature, 585, 357, doi: 10.1038/s41586-020-2649-2

Harrison, C. M., Alexander, D. M., Mullaney, J. R., & Swinbank, A. M. 2014, MNRAS, 441, 3306, doi: 10.1093/mnras/stu515

Hatano, S., Kokubo, M., Ouchi, M., et al. 2026, ApJ, 997, 241, doi: 10.3847/1538-4357/ae29aa

Herenz, E. C., Inoue, J., Salas, H., et al. 2023a, A&A, 670, A121, doi: 10.1051/0004-6361/202244930

Herenz, E. C., Inoue, J., Salas, H., et al. 2023b,, VizieR On-line Data Catalog: J/A+A/670/A121. Originally published in: 2023A&A...670A.121H doi: 10.26093/cds/vizier.36700121

Hernandez, S., Smith, L. J., Jones, L. H., et al. 2025, ApJ, 983, 154, doi: 10.3847/1538-4357/adba5d

Hillier, D. J., Davidson, K., Ishibashi, K., & Gull, T. 2001, ApJ, 553, 837, doi: 10.1086/320948

Hu, C.-Y., Zhukovska, S., Somerville, R. S., & Naab, T. 2019, MNRAS, 487, 3252, doi: 10.1093/mnras/stz1481
Huang, C., & Chevalier, R. A. 2018, MNRAS, 475, 1261, doi: 10.1093/mnras/stx3163
Humphreys, R. M., & Davidson, K. 1994, PASP, 106, 1025, doi: 10.1086/133478
Humphreys, R. M., Davidson, K., Jones, T. J., et al. 2012, ApJ, 760, 93, doi: 10.1088/0004-637X/760/1/93
Humphreys, R. M., & Martin, J. C. 2012, in Astrophysics and Space Science Library, Vol. 384, Eta Carinae and the Supernova Impostors, ed. K. Davidson & R. M. Humphreys, 1, doi: 10.1007/978-1-4614-2275-4_1
Hunt, L. K., Testi, L., Casasola, V., et al. 2014, A&A, 561, A49, doi: 10.1051/0004-6361/201322739
Hunter, J. D. 2007, Computing in Science & Engineering, 9, 90, doi: 10.1109/MCSE.2007.55
Inayoshi, K., & Ichikawa, K. 2024, ApJL, 973, L49, doi: 10.3847/2041-8213/ad74e2
Inayoshi, K., & Maiolino, R. 2025, ApJL, 980, L27, doi: 10.3847/2041-8213/adaebd
Ishibashi, K., Gull, T. R., Davidson, K., et al. 2003, AJ, 125, 3222, doi: 10.1086/375306
Ivezic, Z., & Elitzur, M. 1997, MNRAS, 287, 799, doi: 10.1093/mnras/287.4.799
Izotov, Y. I., Guseva, N. G., Fricke, K. J., & Papaderos, P. 2009, A&A, 503, 61, doi: 10.1051/0004-6361/200911965
Izotov, Y. I., & Thuan, T. X. 1999, ApJ, 511, 639, doi: 10.1086/306708
Izotov, Y. I., Thuan, T. X., Guseva, N. G., & Liss, S. E. 2018, MNRAS, 473, 1956, doi: 10.1093/mnras/stx2478
James, B. L., Tsamis, Y. G., Barlow, M. J., et al. 2009, MNRAS, 398, 2, doi: 10.1111/j.1365-2966.2009.15172.x
Johansson, S., & Letokhov, V. S. 2005, MNRAS, 364, 731, doi: 10.1111/j.1365-2966.2005.09605.x
Johnson, D. R. H., Barlow, M. J., Drew, J. E., & Brinks, E. 1992, MNRAS, 255, 261, doi: 10.1093/mnras/255.2.261
Johnson, K. E., Hunt, L. K., & Reines, A. E. 2009, AJ, 137, 3788, doi: 10.1088/0004-6256/137/4/3788
Juodžbalis, I., Ji, X., Maiolino, R., et al. 2024, MNRAS, 535, 853, doi: 10.1093/mnras/stae2367
Juodžbalis, I., Maiolino, R., Baker, W. M., et al. 2025, arXiv e-prints, arXiv:2504.03551, doi: 10.48550/arXiv.2504.03551
Kehrig, C., Vílchez, J. M., Guerrero, M. A., et al. 2018, MNRAS, 480, 1081, doi: 10.1093/mnras/sty1920
Kennicutt, R. C., & Evans, N. J. 2012, ARA&A, 50, 531, doi: 10.1146/annurev-astro-081811-125610
Kenyon, S. J., & Gallagher, III, J. S. 1985, ApJ, 290, 542, doi: 10.1086/163010
Kimm, T., Haehnelt, M., Blaizot, J., et al. 2018, MNRAS, 475, 4617, doi: 10.1093/mnras/sty126
Kobulnicky, H. A., Skillman, E. D., Roy, J.-R., Walsh, J. R., & Rosa, M. R. 1997, ApJ, 477, 679, doi: 10.1086/303742
Kojima, T., Ouchi, M., Rauch, M., et al. 2021, ApJ, 913, 22, doi: 10.3847/1538-4357/abec3d
Kroupa, P. 2001, MNRAS, 322, 231, doi: 10.1046/j.1365-8711.2001.04022.x
Lamers, H. J. G. L. M., Nota, A., Panagia, N., Smith, L. J., & Langer, N. 2001, ApJ, 551, 764, doi: 10.1086/320229
Lawrence, A. 1982, Nature, 295, 509, doi: 10.1038/295509a0
Leitherer, C., Schaerer, D., Goldader, J. D., et al. 1999, ApJS, 123, 3, doi: 10.1086/313233
Luridiana, V., Morisset, C., & Shaw, R. A. 2013,, Astrophysics Source Code Library, record ascl:1304.021 http://ascl.net/1304.021
Luridiana, V., Morisset, C., & Shaw, R. A. 2015, A&A, 573, A42, doi: 10.1051/0004-6361/201323152
Madden, S. C., Galliano, F., Jones, A. P., & Sauvage, M. 2006, A&A, 446, 877, doi: 10.1051/0004-6361:20053890
Maeder, A., & Meynet, G. 2001, A&A, 373, 555, doi: 10.1051/0004-6361:20010596
Maeder, A., Przybilla, N., Nieva, M.-F., et al. 2014, A&A, 565, A39, doi: 10.1051/0004-6361/201220602
Martin, J. C., Davidson, K., Humphreys, R. M., Hillier, D. J., & Ishibashi, K. 2006, ApJ, 640, 474, doi: 10.1086/500038
McCully, C., Crawford, S., Kovacs, G., et al. 2018,, v1.0.5 Zenodo, doi: 10.5281/zenodo.1482019
McKee, C. 1989, in IAU Symposium, Vol. 135, Interstellar Dust, ed. L. J. Allamandola & A. G. G. M. Tielens, 431
Mehner, A. 2011, PhD thesis, University of Minnesota, Twin Cities
Mehner, A., Davidson, K., Ferland, G. J., & Humphreys, R. M. 2010, ApJ, 710, 729, doi: 10.1088/0004-637X/710/1/729
Mehner, A., Davidson, K., Humphreys, R. M., et al. 2015, A&A, 578, A122, doi: 10.1051/0004-6361/201425522
Méndez-Delgado, J. E., Kreckel, K., Esteban, C., et al. 2024, A&A, 690, A248, doi: 10.1051/0004-6361/202450928
Meynet, G., & Maeder, A. 2002, A&A, 390, 561, doi: 10.1051/0004-6361:20020755
Mingozzi, M., Garcia del Valle-Espinosa, M., James, B. L., et al. 2025, ApJ, 985, 253, doi: 10.3847/1538-4357/adc996
Morisset, C. 2013,, Astrophysics Source Code Library, record ascl:1304.020
Moriya, T. J., Maeda, K., Taddia, F., et al. 2013, MNRAS, 435, 1520, doi: 10.1093/mnras/stt1392

Morrissey, P., Matuszewski, M., Martin, D. C., et al. 2018, ApJ, 864, 93, doi: 10.3847/1538-4357/aad597
Murray, N., Ménard, B., & Thompson, T. A. 2011, ApJ, 735, 66, doi: 10.1088/0004-637X/735/1/66
Murray, N., Quataert, E., & Thompson, T. A. 2005, ApJ, 618, 569, doi: 10.1086/426067
Nagao, T., Maiolino, R., & Marconi, A. 2006, A&A, 447, 863, doi: 10.1051/0004-6361:20054127
Nakane, M., Ouchi, M., Nakajima, K., et al. 2024, ApJ, 976, 122, doi: 10.3847/1538-4357/ad84e8
Nava, A., Casebeer, D., Henry, R. B. C., & Jevremovic, D. 2006, ApJ, 645, 1076, doi: 10.1086/504416
Nebrin, O., Smith, A., Lorinc, K., et al. 2025, MNRAS, 537, 1646, doi: 10.1093/mnras/staf038
Neill, D., Matuszewski, M., Martin, C., Brodheim, M., & Rizzi, L. 2023,, Astrophysics Source Code Library, record ascl:2301.019
Netzer, H., & Penston, M. V. 1976, MNRAS, 174, 319, doi: 10.1093/mnras/174.2.319
Newville, M., Otten, R., Nelson, A., et al. 2021,, 1.0.3, Zenodo Zenodo, doi: 10.5281/zenodo.5570790
Osterbrock, D. E. 1977, ApJ, 215, 733, doi: 10.1086/155407
Osterbrock, D. E. 1988, PASP, 100, 412, doi: 10.1086/132188
Osterbrock, D. E., & Ferland, G. J. 2006, Astrophysics of gaseous nebulae and active galactic nuclei
Pacucci, F., Nguyen, B., Carniani, S., Maiolino, R., & Fan, X. 2023, ApJL, 957, L3, doi: 10.3847/2041-8213/ad0158
Pagel, B. E. J. 2009, Nucleosynthesis and Chemical Evolution of Galaxies (Cambridge University Press)
pandas development team, T. 2020,, latest Zenodo, doi: 10.5281/zenodo.3509134
Papaderos, P., Izotov, Y. I., Guseva, N. G., Thuan, T. X., & Fricke, K. J. 2006, A&A, 454, 119, doi: 10.1051/0004-6361:20065110
Pascale, M., & Dai, L. 2024, ApJ, 976, 166, doi: 10.3847/1538-4357/ad7732
Peimbert, M., & Costero, R. 1969, Boletin de los Observatorios Tonantzintla y Tacubaya, 5, 3
Peng, Z., & Li, Y. 2024,, 0.1.3-alpha Zenodo, doi: 10.5281/zenodo.13782314
Peng, Z., Martin, C. L., Chen, Z., et al. 2025, ApJ, 981, 171, doi: 10.3847/1538-4357/ada606
Pilyugin, L. S., Grebel, E. K., & Mattsson, L. 2012, MNRAS, 424, 2316, doi: 10.1111/j.1365-2966.2012.21398.x
Pittard, J. M., & Corcoran, M. F. 2002, A&A, 383, 636, doi: 10.1051/0004-6361:20020025
Ploeckinger, S., & Schaye, J. 2020, MNRAS, 497, 4857, doi: 10.1093/mnras/staa2172
Prantzos, N., Abia, C., Limongi, M., Chieffi, A., & Cristallo, S. 2018, MNRAS, 476, 3432, doi: 10.1093/mnras/sty316
Prestwich, A. H., Tsantaki, M., Zezas, A., et al. 2013, ApJ, 769, 92, doi: 10.1088/0004-637X/769/2/92
Prochaska, J. X., Hennawi, J., Cooke, R., et al. 2020,, v1.0.0 Zenodo, doi: 10.5281/zenodo.3743493
Prusinski, N. Z., & Chen, Y. 2024,, Astrophysics Source Code Library, record ascl:2404.003
Prusinski, N. Z., Steidel, C. C., & Chen, Y. 2025, arXiv e-prints, arXiv:2503.20037, doi: 10.48550/arXiv.2503.20037
Przybilla, N., Firnstein, M., Nieva, M. F., Meynet, G., & Maeder, A. 2010, A&A, 517, A38, doi: 10.1051/0004-6361/201014164
Quataert, E., Fernández, R., Kasen, D., Klion, H., & Paxton, B. 2016, MNRAS, 458, 1214, doi: 10.1093/mnras/stw365
Reines, A. E., Johnson, K. E., & Hunt, L. K. 2008, AJ, 136, 1415, doi: 10.1088/0004-6256/136/4/1415
Reines, A. E., & Volonteri, M. 2015, ApJ, 813, 82, doi: 10.1088/0004-637X/813/2/82
Richardson, C. T., Wels, J., Garofali, K., et al. 2025, ApJ, 993, 154, doi: 10.3847/1538-4357/adf215
Rodríguez, M., & Rubin, R. H. 2005, ApJ, 626, 900, doi: 10.1086/429958
Rodríguez-Ardila, A., Prieto, M. A., Viegas, S., & Gruenwald, R. 2006, ApJ, 653, 1098, doi: 10.1086/508864
Salehirad, S., Reines, A. E., & Molina, M. 2025, ApJ, 979, 26, doi: 10.3847/1538-4357/ad9a57
Schlafly, E. F., & Finkbeiner, D. P. 2011, The Astrophysical Journal, 737, 103, doi: 10.1088/0004-637X/737/2/103
Senchyna, P., Plat, A., Stark, D. P., et al. 2024, ApJ, 966, 92, doi: 10.3847/1538-4357/ad235e
Shappee, B. J., Prieto, J. L., Grupe, D., et al. 2014, ApJ, 788, 48, doi: 10.1088/0004-637X/788/1/48
Skillman, E. D., Salzer, J. J., Berg, D. A., et al. 2013, AJ, 146, 3, doi: 10.1088/0004-6256/146/1/3
Smith, N. 2006, ApJ, 644, 1151, doi: 10.1086/503766
Smith, N. 2008, Nature, 455, 201, doi: 10.1038/nature07269
Smith, N. 2013, MNRAS, 429, 2366, doi: 10.1093/mnras/sts508
Smith, N. 2017a, in Handbook of Supernovae, ed. A. W. Alsabti & P. Murdin (Springer International Publishing), 403, doi: 10.1007/978-3-319-21846-5_38
Smith, N. 2017b, Philosophical Transactions of the Royal Society of London Series A, 375, 20160268, doi: 10.1098/rsta.2016.0268
Smith, N., & Morse, J. A. 2004, ApJ, 605, 854, doi: 10.1086/382671

Smith, N., Andrews, J. E., Rest, A., et al. 2018, MNRAS, 480, 1466, doi: 10.1093/mnras/sty1500
Soto, K. T., Lilly, S. J., Bacon, R., Richard, J., & Conseil, S. 2016, MNRAS, 458, 3210, doi: 10.1093/mnras/stw474
Storey, P. J., & Hummer, D. G. 1995, Monthly Notices of the Royal Astronomical Society, 272, 41, doi: 10.1093/mnras/272.1.41
Storey, P. J., & Zeippen, C. J. 2000, MNRAS, 312, 813, doi: 10.1046/j.1365-8711.2000.03184.x
Thompson, R. I., Sauvage, M., Kennicutt, R. C., et al. 2009, ApJ, 691, 1068, doi: 10.1088/0004-637X/691/2/1068
Thompson, T. A., & Heckman, T. M. 2024, arXiv e-prints, arXiv:2406.08561. https://arxiv.org/abs/2406.08561
Thompson, T. A., Quataert, E., Zhang, D., & Weinberg, D. H. 2016, MNRAS, 455, 1830, doi: 10.1093/mnras/stv2428
Thuan, T. X., Bauer, F. E., Papaderos, P., & Izotov, Y. I. 2004, ApJ, 606, 213, doi: 10.1086/382949
Timmes, F. X., Woosley, S. E., & Weaver, T. A. 1995, ApJS, 98, 617, doi: 10.1086/192172
Tinsley, B. M. 1980, FCPh, 5, 287, doi: 10.48550/arXiv.2203.02041
Ulrich, M.-H., Maraschi, L., & Urry, C. M. 1997, ARA&A, 35, 445, doi: 10.1146/annurev.astro.35.1.445
van Dokkum, P. G. 2001, PASP, 113, 1420, doi: 10.1086/323894
van Marle, A. J., Smith, N., Owocki, S. P., & van Veelen, B. 2010, MNRAS, 407, 2305, doi: 10.1111/j.1365-2966.2010.16851.x
Villar Martín, M., Bellocchi, E., Stern, J., et al. 2015, MNRAS, 454, 439, doi: 10.1093/mnras/stv1864
Vink, J. S. 2023, A&A, 679, L9, doi: 10.1051/0004-6361/202347827
Virtanen, P., Gommers, R., Oliphant, T. E., et al. 2020, Nature Methods, 17, 261, doi: 10.1038/s41592-019-0686-2
Weis, K., & Bomans, D. J. 2020, Galaxies, 8, 20, doi: 10.3390/galaxies8010020
Welch, B., Rivera-Thorsen, T. E., Rigby, J. R., et al. 2025, ApJ, 980, 33, doi: 10.3847/1538-4357/ada76c
Wolf, B. 1989, A&A, 217, 87
Woo, J.-H., Bae, H.-J., Son, D., & Karouzos, M. 2016, ApJ, 817, 108, doi: 10.3847/0004-637X/817/2/108
Xu, C., McCully, C., Dong, B., Howell, D. A., & Sen, P. 2023, ApJ, 942, 73, doi: 10.3847/1538-4357/ac9d91
Xu, X., Heckman, T., Henry, A., et al. 2022, ApJ, 933, 222, doi: 10.3847/1538-4357/ac6d56
Yanagisawa, H., Ouchi, M., Watanabe, K., et al. 2024, ApJ, 974, 266, doi: 10.3847/1538-4357/ad72ec
Zakamska, N. L., Strauss, M. A., Krolik, J. H., et al. 2003, AJ, 126, 2125, doi: 10.1086/378610